

A Reduced Basis Method for a PDE-constrained optimization formulation in Discrete Fracture Network flow simulations

Original

A Reduced Basis Method for a PDE-constrained optimization formulation in Discrete Fracture Network flow simulations / Berrone, S.; Vicini, F.. - In: COMPUTERS & MATHEMATICS WITH APPLICATIONS. - ISSN 0898-1221. - ELETTRONICO. - 99:(2021), pp. 182-194. [10.1016/j.camwa.2021.08.006]

Availability:

This version is available at: 11583/2949156 since: 2022-01-14T11:47:07Z

Publisher:

Elsevier Ltd

Published

DOI:10.1016/j.camwa.2021.08.006

Terms of use:

This article is made available under terms and conditions as specified in the corresponding bibliographic description in the repository

Publisher copyright

(Article begins on next page)

A Reduced Basis Method for a PDE-constrained optimization formulation in Discrete Fracture Network flow simulations [☆]

S. Berrone^{a,b}, F. Vicini^{a,b,*}

^a*Dipartimento di Scienze Matematiche, Politecnico di Torino
Corso Duca degli Abruzzi 24, Torino, 10129, Italy*

^b*Member of the INdAM research group GNCS*

Abstract

In classic Reduced Basis (RB) framework, we propose a new technique for the offline greedy error analysis which relies on a residual-based a posteriori error estimator. This approach is as an alternative to classical a posteriori RB estimators, avoiding a discrete inf-sup lower bound estimate. We try to use less common ingredients of the RB framework to retrieve a better approximation of the RB error, such as the estimation of the distance between the continuous solution and the reduced one. In particular we focus on the application of the reduction model for the flow simulations in underground fractured media, in which high accurate simulations suffer for the complexity of the domain geometry. Finally, some numerical tests are assessed to confirm the viability and the efficacy of the technique proposed.

Keywords: Discrete Fracture Network flow simulations, Reduced Basis Method, Simulations in complex geometries, Mesh adaptivity, A posteriori error estimates, Adaptivity

1. Introduction

1 Given a partial differential equation (PDE) dependent from a set of parameters, the
2 Reduced Basis Method (RBM) is a well known and valid technique to generate a nu-
3 merical solution dependent on a set of parameters from a linear combination of a small
4 group of detailed high fidelity solutions, each one simulated from a selected parameter
5 value. The selection of this special sub-set of solutions is usually performed resorting
6 to an error analysis on a larger training set of solutions, called “snapshots”. According
7

[☆]This research has been partially supported by PRIN-MIUR projects 201744KLJL_004 and 201752HKH8, and by the MIUR project “Dipartimenti di Eccellenza 2018-2022” (CUP E11G18000350001). Computational resources were partially provided by HPC@POLITO (<https://hpc.polito.it/>) and SMARTDATA@POLITO (<https://smartdata.polito.it/>).

*Corresponding author

Email addresses: stefano.berrone@polito.it (S. Berrone), fabio.vicini@polito.it (F. Vicini)

8 to [1, 2, 3], standard techniques for RB offline greedy error analysis relies on the qual-
9 ity of the high fidelity solutions, thus snapshots should be very accurate; moreover, the
10 RB a posteriori error estimators strongly depend on the value of the condition number
11 of the matrix of the high fidelity problem. Some problems in modern applied engi-
12 neering, such as the simulation of underground phenomena in fractured media, hardly
13 satisfy the properties required by classical RB a posteriori estimators. Fracture net-
14 work geometries are usually generated from random probability distributions yielding
15 to strong geometrical complexities on the domains. This results in hard difficulties in
16 conforming mesh generation, that is sometime infeasible or yields to a huge number of
17 unknowns to fit the geometrical constraints, also where the solution does not display
18 significant behaviours. A variety of strategies are proposed in literature to overcome
19 these problems, such as [4, 5, 6] in which little geometry modifications are performed,
20 or such as [7, 8, 9, 10] in which the authors try to relax or remove the conformity con-
21 straints on fracture intersections. In the present work we focus on a PDE-constrained
22 optimization method applied to Discrete Fracture Networks (DFN), introduced in [11]
23 and validated in [12], to avoid the geometrical complexities in the generation of the
24 mesh on the fracture intersections and to remarkably reduce the number of unknowns
25 of the discrete problem. We show that classic RBM error estimators are not effective
26 to the fracture network problem when using non-conforming meshes due to the small
27 value of the inf-sup constant of the discretized problem [13]. Moreover, we try to pro-
28 pose an alternative RBM greedy offline error estimator to build a reliable RB space
29 thanks to a residual-based a posteriori error estimate available in [14] and [15] associ-
30 ated to the optimization method. Section 2 introduces the greedy approach proposed.
31 In Section 3 we report the DFN variational parametrized PDE problem. Finally, Sec-
32 tion 4 introduces the reduction applied to the DFN discrete problem and the greedy
33 a posteriori analysis. The error estimations is validated with some numerical tests in
34 Section 5.

35 2. RB Error Estimates

36 The definition of a RB a posteriori error estimators is fundamental for the reli-
37 ability of the RB method, see for example [1, 2, 16]. Given a set of parameters
38 $\mu = (\mu_1, \dots, \mu_p) \in \mathcal{P} \subset \mathbb{R}^p$ and two Hilbert spaces \mathcal{X} and \mathcal{Y} on \mathbb{R} along with their dual
39 \mathcal{X}^* and \mathcal{Y}^* , we consider a parametrized variational numerical problem $P : \mathcal{P} \times D \rightarrow \mathcal{X}$
40 on the domain $D \subset \mathbb{R}^d$

$$a(w, v; \mu) = f(v; \mu) \quad \forall v \in \mathcal{Y}, \quad (1)$$

41 with $a(\cdot, \cdot; \mu) : \mathcal{X} \times \mathcal{Y} \rightarrow \mathbb{R}$ bilinear form and $f(\cdot; \mu) \in \mathcal{Y}^*$ bounded linear functional
42 on \mathcal{Y} for each $\mu \in \mathcal{P}$. We denote by $(\cdot, \cdot)_{\mathcal{X}}$ the inner product over the space \mathcal{X} and
43 by $\|\cdot\|_{\mathcal{X}}^2 = (\cdot, \cdot)_{\mathcal{X}}$ the induced norm. Moreover, ${}_{\mathcal{Y}^*}\langle f, v \rangle_{\mathcal{Y}}$ denotes the duality pairing
44 between \mathcal{Y}^* and \mathcal{Y} . In what follows we assume the well-posedness of the problem (1)
45 with unique solution $w(\mu) \in \mathcal{X}$ for all $\mu \in \mathcal{P}$. For the Nečas theorem, this is equivalent
46 [17] to guarantee the existence of a finite continuity upper bound constant $\gamma_{UB} > 0$ s.t.
47 $\gamma(\mu) = \sup_{w \in \mathcal{X}} \sup_{v \in \mathcal{Y}} \frac{a(w, v; \mu)}{\|w\|_{\mathcal{X}} \|v\|_{\mathcal{Y}}} \leq \gamma_{UB}$, the inf-sup condition $\inf_{v \in \mathcal{Y}} \sup_{w \in \mathcal{X}} \frac{a(w, v; \mu)}{\|w\|_{\mathcal{X}} \|v\|_{\mathcal{Y}}} > 0$

48 and a finite inf-sup lower bound constant $\beta_{LB} > 0$ s.t.

$$\beta(\mu) = \inf_{w \in \mathcal{X}} \sup_{v \in \mathcal{Y}} \frac{a(w, v; \mu)}{\|w\|_{\mathcal{X}} \|v\|_{\mathcal{Y}}} \geq \beta_{LB}. \quad (2)$$

49 Under these assumptions, choosing $\mathcal{X}_\delta \subset \mathcal{X}$ and $\mathcal{Y}_\delta \subset \mathcal{Y}$ as closed subspaces of
50 finite dimension δ , we approximate the continuous problem (1) with the following weak
51 discrete problem $P_\delta : \mathcal{P} \times D \rightarrow \mathcal{X}_\delta$

$$a(w_\delta, v; \mu) = f(v; \mu) \quad \forall v \in \mathcal{Y}_\delta. \quad (3)$$

52 Let $w_\delta(\mu) \in \mathcal{X}_\delta$ be the unique solution of problem (3) and $w_N(\mu) \in \mathcal{X}_N \subseteq \mathcal{X}_\delta$ the
53 solution of the reduced problem $P_N : \mathcal{P} \times D \rightarrow \mathcal{X}_N$

$$a_N(w_N, v; \mu) = f_N(v; \mu) \quad \forall v \in \mathcal{Y}_N, \quad (4)$$

54 being $\mathcal{X}_N \subset \mathcal{X}_\delta$ and $\mathcal{Y}_N \subset \mathcal{Y}_\delta$ subspaces of dimension N . Classical a posteriori RB
55 estimators have the goal to approximate for each $\mu \in \mathcal{P}$ the norm of the error $e_{\delta, N} :
56 \mathcal{X}_\delta \times \mathcal{X}_N \rightarrow \mathcal{X}_\delta$ s.t.

$$e_{\delta, N}(w_\delta, w_N; \mu) := w_\delta(\mu) - \mathbb{V} w_N(\mu), \quad (5)$$

57 being $\mathbb{V} \in \mathbb{R}^{\delta \times N}$ the column-wise collection of the orthonormal basis $\{\zeta_n\}_{n \in \{1, \dots, N\}}$ of \mathcal{X}_N .
58 Assuming the well-posedness of problem (3) for each $\mu \in \mathcal{P}$ there exists a discrete inf-
59 sup lower bound $\beta_{\delta, LB} > 0$ s.t.

$$\beta_\delta(\mu) = \inf_{w \in \mathcal{X}_\delta} \sup_{v \in \mathcal{Y}_\delta} \frac{a(w, v; \mu)}{\|w\|_{\mathcal{X}} \|v\|_{\mathcal{Y}}} \geq \beta_{\delta, LB}. \quad (6)$$

60 Following [17], classical RB theory introduces a posteriori estimator $\Delta_N : \mathcal{P} \times \mathcal{X}_N \rightarrow
61 \mathbb{R}$, defined $\forall \mu \in \mathcal{P}$ as

$$\Delta_N(w_N; \mu) := \frac{\|R_\delta(\mathbb{V} w_N; \mu)\|_{\mathcal{Y}^*}}{\beta_\delta(\mu)}, \quad (7)$$

62 where we indicate with $R_\delta : \mathcal{P} \times \mathcal{X}_\delta \rightarrow \mathbb{R} \in \mathcal{Y}_\delta^*$ the discrete residual $\forall v \in \mathcal{Y}_\delta$

$${}_{\mathcal{Y}^*} \langle R_\delta(w_\delta; \mu), v \rangle_{\mathcal{Y}} := f(v; \mu) - a(w_\delta, v; \mu). \quad (8)$$

63 For the sake of notational simplicity, $\Delta_N(w_N; \mu)$ and $e_{\delta, N}(w_\delta, w_N; \mu)$ will be shortened
64 to $\Delta_N(\cdot; \mu)$ and $e_{\delta, N}(\cdot; \mu)$. In order to evaluate the reliability of (7) we introduce the
65 effectivity index $\eta_N(\mu) := \frac{\Delta_N(\cdot; \mu)}{\|e_{\delta, N}(\cdot; \mu)\|_{\mathcal{X}}}$. Using the discrete continuity constant $\gamma_\delta(\mu)$, from
66 classical theory follows

$$1 \leq \eta_N(\mu) \leq \frac{\gamma_\delta(\mu)}{\beta_\delta(\mu)} = \kappa_\delta(\mu), \quad (9)$$

67 being $\kappa_\delta(\mu)$ the condition number of the matrix associated to the high fidelity problem
68 P_δ . The error estimation $\|e_{\delta, N}(\cdot; \mu)\|_{\mathcal{X}} \leq \Delta_N(w_N; \mu)$ is the base for most of the RB
69 greedy algorithms for the construction of the RB space \mathcal{X}_N , starting from a sufficiently
70 large sample set $S_M = \{\mu^1, \dots, \mu^M\} \subseteq \mathcal{P}$.

71 Algorithm 1 reports the steps required to obtain matrix \mathbb{V} we introduced in (5) for
 72 a given a tolerance $\varepsilon_N > 0$, see [1, 16, 17]. The quantity (7) is computed using

$$\Delta_{N,I}(w_N; \mu) := \frac{\|R_\delta(\mathbb{V}w_N; \mu)\|_{\mathcal{Y}}}{\beta_{\delta,I}(\mu)} \quad (10)$$

73 with the use of a suitable interpolatory approximation $\beta_{\delta,I} : \mathcal{P} \rightarrow \mathbb{R}$ in place of the
 74 exact value $\beta_\delta(\mu)$ for each $\mu \in \mathcal{P}$, [18]. Other reliable techniques to approximate the
 inf-sup constants may be used, such as the SCM introduced in [19].

Algorithm 1 RB Greedy Space Basis Construction - Classic

Input: $\varepsilon_N > 0$, $S_M = \{\mu^1, \dots, \mu^M\} \subseteq \mathcal{P}$, $\beta_{\delta,I} : \mathcal{P} \rightarrow \mathbb{R}$

Output: $N \geq 0$, $\mathbb{V} = [\zeta_1, \dots, \zeta_N] \in \mathbb{R}^{\delta \times N}$

1: Initialize $\mathbb{V} = []$, $N = 0$, $\delta_N = \varepsilon_N + 1$, $\mu_s^1 = \text{rand}(S_M)$

2: **while** $N < M \wedge \delta_N > \varepsilon_N$ **do**

3: $N = N + 1$

4: Compute $w_\delta(\mu_s^N)$ solving P_δ

5: $\zeta_N = \text{GramSchmidt}(\mathbb{V}, w_\delta(\mu_s^N))$

6: $\mathbb{V} = [\mathbb{V}, \zeta_N]$

7: Compute $\mathbb{S}_{N,M} = [w_N(\mu^1), \dots, w_N(\mu^M)] \in \mathbb{R}^{N \times M}$ solving P_N

8: $\mu_s^{N+1} = \arg \max_{\mu \in S_M} \Delta_{N,I}(w_N; \mu)$

9: $\delta_N = \Delta_{N,I}(w_N; \mu_s^{N+1}) / \|w_N(\mu_s^{N+1})\|_X$

10: **end while**

75 Our target is to provide an estimate of $e_{\delta,N}(\cdot; \mu)$ for problems P_δ in which the dis-
 76 crete inf-sup $\beta_\delta(\mu)$ is very small $\forall \mu \in \mathcal{P}$ and the condition number $\kappa_\delta(\mu)$ grows rapidly
 77 when the complexity of the problem increases. Other authors perform a similar task,
 78 such as the hierarchical methods introduced in [2]. However, in DFN flow simula-
 79 tion with no conformity requirements on the mesh at fracture intersections, accurate
 80 high-fidelity solutions w_δ are not easy to obtain, [13]. We introduce for all $\mu \in \mathcal{P}$ the
 81 quantities $e_N : \mathcal{X} \times \mathcal{X}_N \rightarrow \mathcal{X}$ and $e_\delta : \mathcal{X} \times \mathcal{X}_\delta \rightarrow \mathcal{X}$ defined by
 82

$$e_N(w, w_N; \mu) := w(\mu) - \mathbb{V}w_N(\mu), \quad e_\delta(w, w_\delta; \mu) := w(\mu) - w_\delta(\mu), \quad (11)$$

83 suitable to measure the distances between the solution of the continuous problem $w(\mu)$
 84 from the reduced one $w_N(\mu)$ and from the discrete one $w_\delta(\mu)$. As we did for (5),
 85 $e_N(w, w_N; \mu)$ and $e_\delta(w, w_\delta; \mu)$ in (11) will be shorten to $e_N(\cdot; \mu)$ and $e_\delta(\cdot; \mu)$. In [20]
 86 and [3], the same quantities are already investigated for similar purposes. Assuming
 87 the mesh for the high fidelity problem fixes, for each parameter $\mu \in \mathcal{P}$ we consider
 88 the triangle formed by $w(\mu)$, $w_\delta(\mu)$ and $w_N(\mu)$. From Figure 1, we can note that when
 89 $\|e_{\delta,N}(\cdot; \mu)\|_X \rightarrow 0$

$$\|e_{\delta,N}(\cdot; \mu)\|_X \approx \left| \|e_\delta(\cdot; \mu)\|_X - \|e_N(\cdot; \mu)\|_X \right|, \quad (12)$$

90 thanks to the cosine rule. Based on this relation, we introduce a new algorithm to build
 91 the RB space which takes in account the distance between the exact solution $w(\mu)$ and

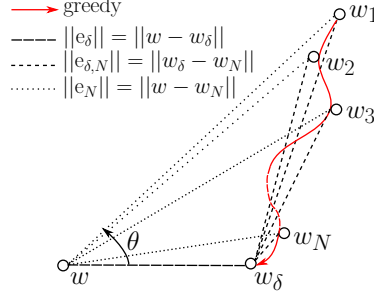


Figure 1: Algorithm 2 - Intuitive explanation

92 the reduced solution $w_N(\mu)$. The residual based a posteriori error estimate [21] ensures
 93 the existence of two positive constants $C^* > 0$ and $C_* > 0$ independent of the mesh
 94 size s.t.

$$C_* \Delta_\delta(w_\delta; \mu) \leq \|e_\delta(w, w_\delta; \mu)\|_{\mathcal{X}} \leq C^* \Delta_\delta(w_\delta; \mu), \quad (13)$$

95 where $\Delta_\delta : \mathcal{P} \times \mathcal{X}_\delta \rightarrow \mathbb{R}$ is a discrete residual-based a posteriori error estimator, [15, 22].
 96 Let us define $\Delta_{\delta,N} : \mathcal{P} \times \mathcal{X}_N \rightarrow \mathbb{R}$ for each $\mu \in \mathcal{P}$ as

$$\Delta_{\delta,N}(w_N; \mu) := \Delta_\delta(\mathbb{V} w_N; \mu). \quad (14)$$

97 The error in (12) can be estimated by

$$\left| \|e_\delta(\cdot; \mu)\|_{\mathcal{X}} - \|e_N(\cdot; \mu)\|_{\mathcal{X}} \right| \approx \left| \Delta_\delta(w_\delta; \mu) - \Delta_{\delta,N}(w_N; \mu) \right|, \quad (15)$$

98 thanks to $\mathcal{X}_N \subseteq \mathcal{X}_\delta$ and to the Petrov-Galerkin orthogonality which holds for (3) and
 99 (4), as shown in [17]. $\Delta_\delta(w_\delta; \mu)$ and $\Delta_{\delta,N}(w_N; \mu)$ will be shortened to $\Delta_\delta(\cdot; \mu)$ and
 100 $\Delta_{\delta,N}(\cdot; \mu)$ in next sections. In estimation (15) we do not include the constants C_* and
 101 C^* because we assume them uniformly bounded with respect to the parameter μ , [22].
 Finally, similar to the approach provided in (10), we introduce a suitable interpola-

Algorithm 2 Greedy RB Space Basis Construction - Exact Solution

Input: $\varepsilon_N > 0$, $S_M = \{\mu^1, \dots, \mu^M\} \subseteq \mathcal{P}$, $\Delta_{\delta,I} : \mathcal{P} \rightarrow \mathbb{R}$

Output: $N \geq 0$, $\mathbb{V} = [\zeta_1, \dots, \zeta_N] \in \mathbb{R}^{\delta \times N}$

- 1: Initialize $\mathbb{V} = []$, $N = 0$, $\delta_N = \varepsilon_N + 1$, $\mu_s^1 = \text{rand}(S_M)$
 - 2: **while** $N < M \wedge \delta_N > \max\{\varepsilon_N, \varepsilon_\delta\}$ **do**
 - 3: $N = N + 1$
 - 4: Compute $w_\delta(\mu_s^N)$ solving P_δ
 - 5: $\zeta_N = \text{GramSchmidt}(\mathbb{V}, w_\delta(\mu_s^N))$
 - 6: $\mathbb{V} = [\mathbb{V}, \zeta_N]$
 - 7: Compute $\mathbb{S}_{N,M} = [w_N(\mu^1), \dots, w_N(\mu^M)] \in \mathbb{R}^{N \times M}$ solving P_N
 - 8: $\mu_s^{N+1} = \arg \max_{\mu \in S_M} |\Delta_{\delta,N}(w_N; \mu_s^{N+1}) - \Delta_{\delta,I}(\mu_s^{N+1})|$
 - 9: $\delta_N = |\Delta_{\delta,N}(w_N; \mu_s^{N+1}) - \Delta_{\delta,I}(\mu_s^{N+1})| / \Delta_{\delta,I}(\mu_s^{N+1})$
 - 10: **end while**
-

102 tion $\Delta_{\delta,I} : \mathcal{P} \rightarrow \mathbb{R}$ in place of the estimator value $\Delta_\delta(\cdot; \mu)$ for each $\mu \in \mathcal{P}$. Then,
 103

104 Algorithm 2 provides the reduced space basis using (15) to capture the maximum vari-
 105 ability of the error avoiding the dependency from the discrete inf-sup constant $\beta_\delta(\mu)$.
 106 Moreover, referring again to Figure 1 and using the triangle inequality

$$\|e_N(\cdot; \mu)\|_{\mathcal{X}} \leq \|e_\delta(\cdot; \mu)\|_{\mathcal{X}} + \|e_{\delta, N}(\cdot; \mu)\|_{\mathcal{X}} \leq (\varepsilon_\delta + \varepsilon_N) \|w_\delta(\cdot; \mu)\|_{\mathcal{X}} \quad (16)$$

107 we can choose the tolerance of the RB method ε_N in the same order of magnitude of
 108 the tolerance to control the high fidelity error ε_δ , to obtain an RBM error proportional
 109 to the discrete one.

110 3. DFN Model

111 In what follows we provide a brief description of the DFN model, which represents
 112 a network of geological fractures on an impervious rock matrix, [15, 23, 24, 25, 22].
 113 The discrete network

$$\mathcal{F} := \bigcup_{i \in \mathcal{I}} F_i \subseteq D \subset \mathbb{R}^3 \quad (17)$$

114 collects all the fractures F_i , $i \in \mathcal{I} = \{1, \dots, I\}$, represented as planar polygons in the
 115 three dimensional domain $D \subset \mathbb{R}^3$. The set of segments collecting all the intersections
 116 between two fractures is denoted by $\mathcal{S} := \bigcup_{m \in \mathcal{M}} S^m$ with $S^m := \bar{F}_i \cap \bar{F}_j$, $m \in \mathcal{M} =$
 117 $\{1, \dots, M\}$; fracture intersections are addressed as “traces” below. A bijective map
 118 $I_S : \mathcal{M} \mapsto \mathcal{I} \times \mathcal{I}$ is directly defined by $I_S(m) = (i, j)$ with $i < j$. As a natural extension
 119 of the notation introduced, $\mathcal{S}_i = \mathcal{S}|_{F_i}$ will denote the subset of traces restricted to F_i
 120 and \mathcal{M}_i their trace’s indices. The network boundary $\partial\mathcal{F}$ is split in the Dirichlet part
 121 Γ_D , with $|\Gamma_D| > 0$ and the Neumann part $\Gamma_N = \partial\mathcal{F} \setminus \Gamma_D$; $b^D \in H^{\frac{1}{2}}(\Gamma_D)$ is imposed
 122 on Γ_D and an homogeneous Neumann conditions is imposed on Γ_N ; see [23] for more
 123 details on non homogeneous Neumann boundary conditions. Finally, on the restricted
 124 sets $\Gamma_{iD} = \Gamma_D|_{F_i}$ the intuitive $b_i^D := b^D|_{\Gamma_{iD}}$ boundary functions are imposed.

125 3.1. The Continuous Problem

126 Out target is the computation of the hydraulic head H ruled by a Darcy’s law on the
 127 full network \mathcal{F} . For each $i \in \mathcal{I}$, let us introduce the functional spaces $V_i^D := H_D^1(F_i) =$
 128 $\{v \in H^1(F_i) : v|_{\Gamma_{iD}} = b_i^D\}$, $V_i := H_0^1(F_i) = \{v \in H^1(F_i) : v|_{\Gamma_{iD}} = 0\}$ and the problem
 129 $H_i \in V_i^D$ s.t. $\forall v \in V_i$

$$\int_{F_i} K_i \nabla H_i \nabla v \, dF = \int_{F_i} Q_i v \, dF + \sum_{m=1}^M \int_{S^m} \left[\frac{\partial H_i}{\partial \hat{\nu}_i^m} \right] v|_{S^m} \, d\gamma. \quad (18)$$

130 K_i represents the fracture hydraulic conductivity tensor that here is assumed to be con-
 131 stant on the fracture F_i , Q_i the source term of the fracture and $\left[\frac{\partial H_i}{\partial \hat{\nu}_i^m} \right]$ the jump of the co-
 132 normal derivative of the hydraulic head along the unit vector $\hat{\nu}_i^m$ of F_i on each $S^m \in \mathcal{S}_i$
 133 with $\frac{\partial H_i}{\partial \hat{\nu}_i^m} = K_i \nabla H_i \cdot \hat{\nu}_i^m$. Finally, two conditions on each $S^m \in \mathcal{S}$ shall be imposed to

134 guarantee the continuity of the hydraulic head on the intersections and the balance of
 135 the normal fluxes; thus, for all $m \in \mathcal{M}$

$$\begin{aligned} H_i|_{S^m} - H_j|_{S^m} &= 0, \\ \left[\frac{\partial H_i}{\partial \hat{v}_i^m} \right] + \left[\frac{\partial H_j}{\partial \hat{v}_j^m} \right] &= 0, \end{aligned} \quad (19)$$

136 with i and j induced by the map $I_S(m)$.

137 The introduced model can be converted into an equivalent optimization problem,
 138 see [11, 15] for further details, introducing the spaces $V := \prod_{i \in \mathcal{I}} V_i^D$, $W_m := \mathbf{H}^{-\frac{1}{2}}(S^m)$
 139 and $W_m^* := \mathbf{H}^{\frac{1}{2}}(S^m) \forall m \in \mathcal{M}$ and the quantity $U_m^i \in W_m$

$$U_m^i := \left[\frac{\partial H_i}{\partial \hat{v}_i^m} \right] + \alpha H_i|_{S^m}, \quad (21)$$

140 with $\alpha > 0$ an arbitrary positive constant introduced for the well posedness of the flow
 141 problem on each F_i . Conditions (19) and (20) can be replaced by the minimization of
 142 the functional $J : V \times W \rightarrow \mathbb{R}$

$$J(H, U) = \sum_{m=1}^M \|H_i|_{S^m} - H_j|_{S^m}\|_{W_m^*}^2 + \|U_i^m + U_j^m - \alpha(H_i|_{S^m} + H_j|_{S^m})\|_{W_m}^2 \quad (22)$$

143 for all $H \in V$ and being $U \in \overline{W} := \prod_{m \in \mathcal{M}} (W_m \times W_m)$. Introducing the following
 144 bilinear forms $a_{F_i} : V_i^D \times V_i \rightarrow \mathbb{R}$ and $a_{S_i} : W_m \times W_m^* \rightarrow \mathbb{R}$

$$a_{F_i}(u, v) := (\nabla u, \nabla v)_{L^2(F_i)}, \quad a_{S_i}(q, s) := \sum_{S^m \in \mathcal{S}_i} w_m^* \langle s, q \rangle_{W_m}. \quad (23)$$

145 Darcy's equation (18) can be shortened applying the constraint functional $G_i : V_i^D \times$
 146 $W_m \times V_i \rightarrow \mathbb{R}$ defined as

$$G_i(H_i, U_i^m, v) = 0 \Leftrightarrow a_{F_i}(K_i H_i, v) + a_{S_i}(\alpha H_i|_{S^m} - U_i^m, v|_{S^m}) - (Q_i, v)_{L^2(F_i)} = 0 \quad (24)$$

147 Thus, the set of equations (18)-(19)-(20) are equivalently replaced [11] by the opti-
 148 mization problem find $H \in V$ s.t.

$$\min_{U \in \overline{W}} J(H, U) \text{ s.t. } G_i(H_i, U_i^m, v) = 0 \quad \forall i \in \mathcal{I}, \quad (25)$$

149 with U the control variable of the problem given by the cartesian product of U_i^m for
 150 all $S^m \in \mathcal{S}_i$ with $i \in \mathcal{I}$. It is possible to reformulate the optimization problem (25),
 151 [15, 22], introducing a Lagrange multiplier $P \in V$, the space $\mathcal{X} := V \times W \times V$ and the
 152 space $\mathcal{Y} := V \times W^* \times V$. A Lagrangian functional $\mathcal{L} : \mathcal{X} \times \mathcal{Y} \rightarrow \mathbb{R}$ can be defined for
 153 $w := (H, U, P) \in \mathcal{X}$, $r := (v, t, q) \in \mathcal{Y}$

$$\begin{aligned} \mathcal{L}(w, r) := & \sum_{i \in \mathcal{I}} a_{F_i}(K_i H_i, v_i) + a_{S_i}(\alpha H_i|_{S^m} - U_i^m, v_i|_{S^m}) + \\ & a_{F_i}(K_i P_i, q_i) - a_{S_i}(H_i|_{S^m} - H_j|_{S^m}, q_i|_{S^m}) + \\ & a_{S_i}(U_i^m + U_j^m - \alpha(H_i|_{S^m} + H_j|_{S^m})) + P_i|_{S^m}, t|_{S^m}) - (Q_i, v_i)_{L^2(F_i)}, \end{aligned} \quad (26)$$

154 where $P_i := P|_{F_i} \in V_i$, $v_i := v|_{F_i} \in V_i$ and $q_i := q|_{F_i} \in V_i$. By referring to [11], problem

$$\mathcal{L}(w, v) = 0, \quad \forall v \in \mathcal{Y} \quad (27)$$

155 has a unique solution $w := (H, U, P) \in \mathcal{X}$ equivalent to the one of the optimization
 156 problem (25) and, thanks to the Nečas theorem, it is possible to prove the inf-sup
 157 condition (2) with the space norm $\|\cdot\|_{\mathcal{X}}$ defined as follows: given $w := (H, U, P) \in \mathcal{X}$

$$\begin{aligned} \|w\|_{\mathcal{X}}^2 := & \sum_{i \in \mathcal{I}} K_i |H_i|_{\mathbb{H}^1(F_i)}^2 + K_i |P_i|_{\mathbb{H}^1(F_i)}^2 + \\ & \sum_{S^m \in \mathcal{S}_i} \left(\|\alpha H_i|_{S^m}\|_{\mathbb{L}^2(S^m)}^2 + \|\alpha P_i|_{S^m}\|_{\mathbb{L}^2(S^m)}^2 + \|U_i^m\|_{\mathbb{H}^{-1/2}(S^m)}^2 \right), \end{aligned} \quad (28)$$

158 with $|\cdot|_{\mathbb{H}^1(F_i)}$ representing the semi-norm in the space $\mathbb{H}^1(F_i)$.

159 3.2. The Discrete Problem

160 Following the approach introduced in [25], the discretization of the problem is
 161 performed independently on each fracture creating an independent mesh \mathcal{T}_i on F_i and a
 162 mesh \mathcal{T}_i^m on each trace S^m in F_i . On each F_i we introduce the finite-dimensional space
 163 $V_{\delta,i} := \text{span}\{\varphi_{i,k}\}_{k \in \{1, \dots, N_i\}} \subset V_i$ of dimension N_i . The set of functions $\{\varphi_{i,\ell}^D\}_{\ell \in \{1, \dots, N_{i,D}\}}$ is
 164 used to discretize the lifting function on the Dirichlet boundary and the space $V_{\delta,i}^D :=$
 165 $V_{\delta,i} \times \text{span}\{\varphi_{i,\ell}^D\}_{\ell \in \{1, \dots, N_{i,D}\}}$ of dimension $N_i^D := N_i + N_{i,D}$ is introduced. In the following,
 166 the contractions $\mathcal{N}_i := \{1, \dots, N_i\}$, $\mathcal{N}_{i,D} := \{N_i + 1, \dots, N_i^D\}$ and $\mathcal{N}_i^D := \{1, \dots, N_i^D\}$ are
 167 used. Similarly, we define on each S^m of F_i the finite-dimensional subspace $W_{\delta,i}^m :=$
 168 $\text{span}\{\psi_{i,\ell}^m\}_{\ell \in \{1, \dots, N_i^m\}} \subset \mathbb{L}^2(S^m) \subset W_m$ of dimension N_i^m . For the sake of notation, in the
 169 following we use the same symbol to denote both the discrete functions and the vectors
 170 of its degree of freedom (DOFs); for example h_i will state both for the function $h_i \in V_{\delta,i}^D$
 171 and the real vector $h_i \in \mathbb{R}^{N_i^D}$. Therefore, the discrete hydraulic head $h_i \in V_{\delta,i}^D$ and the
 172 discrete control variable $u_i^m \in W_{\delta,i}^m$ are naturally defined. Finally, we define the discrete
 173 hydraulic head of the network as $h := (h_1, \dots, h_I) \in V_{\delta} := \prod_{i \in \mathcal{I}} V_{\delta,i}^D$ of dimension
 174 $N_{\mathcal{F}} = \sum_{i \in \mathcal{I}} N_i^D$ and the discrete control variable of the network $u := (u^1, \dots, u^M) \in$
 175 $W_{\delta} := \prod_{m \in \mathcal{M}} (W_{\delta,i}^m \times W_{\delta,j}^m)$ of dimension $N^S = \sum_{m \in \mathcal{M}} (N_i^m + N_j^m)$, having set $u^m =$
 176 $(u_j^m, u_j^m) \in W_{\delta,i}^m \times W_{\delta,j}^m$, with i and j taken from the map $I_S(m)$. The discrete counterpart
 177 of Darcy's equation in (25) can be deduced introducing the matrices $\mathbb{A}_{F_i}, \mathbb{A}_{F_i}^D \in \mathbb{R}^{N_i^D \times N_i^D}$
 178 and $\mathbb{A}_{S_i}, \mathbb{A}_{S_i}^D \in \mathbb{R}^{N_i^D \times N_i^D}$ defined by

$$\begin{aligned} \mathbb{A}_{F_i}|_{k\ell} = & \begin{cases} a_{F_i}(\varphi_{i,k}, \varphi_{i,\ell}) & k, \ell \in \mathcal{N}_i \\ 1 & k = \ell \in \mathcal{N}_{i,D} \\ 0 & \text{otherwise} \end{cases}, \mathbb{A}_{F_i}^D|_{k\ell} = \begin{cases} a_{F_i}(\varphi_{i,k}, \varphi_{i,\ell}^D) & k \in \mathcal{N}_i, \ell \in \mathcal{N}_{i,D} \\ -1 & k = \ell \in \mathcal{N}_{i,D} \\ 0 & \text{otherwise} \end{cases} \\ \mathbb{A}_{S_i}|_{k\ell} = & \begin{cases} a_{S_i}(\varphi_{i,k}|_{S^m}, \varphi_{i,\ell}|_{S^m}) & k, \ell \in \mathcal{N}_i \\ 0 & \text{otherwise} \end{cases}, \mathbb{A}_{S_i}^D|_{k\ell} = \begin{cases} a_{S_i}(\varphi_{i,k}|_{S^m}, \varphi_{i,\ell}^D|_{S^m}) & k \in \mathcal{N}_i, \ell \in \mathcal{N}_{i,D} \\ 0 & \text{otherwise} \end{cases}. \end{aligned} \quad (29)$$

179 The matrix $\mathcal{B}_i \in \mathbb{R}^{N_i^D \times N^S}$ is also introduced to collect the integrals of the product of
 180 basis functions $\{\varphi_{i,k}|_{S^m}\}_{k \in \{1, \dots, N_i^D\}}$ with $\{\psi_{i,\ell}^m\}_{\ell \in \{1, \dots, N_i^m\}}$ for all $S^m \in \mathcal{S}_i$. Therefore, for

181 each $i \in \mathcal{I}$ we obtain the discrete version of (24), $G_{\delta,i}(h, u) : V_\delta \times W_\delta \rightarrow \mathbb{R}$ with
 182 $G_{\delta,i}(h, u) := \mathbb{A}_i h_i - q_i + \mathbb{A}_i^D h_i^D - \mathcal{B}_i u$, with matrix $\mathbb{A}_i = K_i \mathbb{A}_{F_i} + \alpha \mathbb{A}_{S_i} \in \mathbb{R}^{N_i^D \times N_i^D}$,
 183 matrix $\mathbb{A}_i^D = K_i \mathbb{A}_{F_i}^D + \alpha \mathbb{A}_{S_i}^D \in \mathbb{R}^{N_i^D \times N_i^D}$, vector $q_i \in \mathbb{R}^{N_i^D}$ the discretization of the forcing
 184 term Q_i and vector $h_i^D \in \mathbb{R}^{N_i^D}$ the evaluation of the Dirichlet boundary conditions b_i^D .
 185 Finally, let us introduce the block-diagonal matrices $\mathbb{A} := \text{diag}(\mathbb{A}_i)_{i \in \mathcal{I}} \in \mathbb{R}^{N_\mathcal{F} \times N_\mathcal{F}}$ and
 186 $\mathbb{A}^D := \text{diag}(\mathbb{A}_i^D)_{i \in \mathcal{I}} \in \mathbb{R}^{N_\mathcal{F} \times N_\mathcal{F}}$, the column-wise collection matrix $\mathcal{B} := (\mathcal{B}_1, \dots, \mathcal{B}_I) \in$
 187 $\mathbb{R}^{N_\mathcal{F} \times N^S}$ and the column vectors $q := (q_1, \dots, q_I)$, $h^D := (h_1^D, \dots, h_I^D) \in \mathbb{R}^{N_\mathcal{F}}$ to obtain
 188 the discrete constraints equation

$$\mathbb{A}h - q + \mathbb{A}^D h^D - \mathcal{B}u = 0, \quad (30)$$

189 simply denoted by $G_\delta(h, u) = 0$. In the discrete framework, the functional (22) can
 190 be written using $L^2(S^m)$ norms in place of W_m and W_m^* norms, obtaining the discrete
 191 functional $J_\delta : V_\delta \times W_\delta \rightarrow \mathbb{R}$

$$J_\delta(h, u) := \frac{1}{2} \left(h^T \mathbb{G}^h h - \alpha h^T \mathbb{B}^h u - \alpha u^T \mathbb{B}^u h + u^T \mathbb{G}^u u \right). \quad (31)$$

192 The matrix $\mathbb{B}^h = (\mathbb{B}^u)^T \in \mathbb{R}^{N_\mathcal{F} \times N^S}$ collects the integrals of the mixed products between
 193 basis functions of V_δ and W_δ and the matrix $\mathbb{G}^u \in \mathbb{R}^{N^S \times N^S}$ is the mass matrix of the
 194 products between the traces basis functions. Furthermore, the matrix $\mathbb{G}^h \in \mathbb{R}^{N_\mathcal{F} \times N_\mathcal{F}}$ is
 195 defined as the sum $\mathbb{G}^h = (\alpha^2 + 1) \mathbb{G}_\mathcal{F}^h + (\alpha^2 - 1) \mathbb{G}_S^h$, with $\mathbb{G}_\mathcal{F}^h \in \mathbb{R}^{N_\mathcal{F} \times N_\mathcal{F}}$ column-wise
 196 combination $\forall S^m \in \mathcal{S}_i$ of matrices $\mathbb{G}_{F_i}^h \in \mathbb{R}^{N_i^D \times N_\mathcal{F}}$

$$(\mathbb{G}_{F_i}^h)_{k\hat{\ell}(i)} = (\varphi_{i,k}^\star |_{S^m}, \varphi_{i,\ell}^\star |_{S^m}) \quad k, \ell \in \mathcal{N}_i^D, \quad (32)$$

197 and $\mathbb{G}_S^h \in \mathbb{R}^{N_\mathcal{F} \times N_\mathcal{F}}$ column-wise combination $\forall S^m \in \mathcal{S}_i$ of matrices $\mathbb{G}_{S^m}^h \in \mathbb{R}^{N_i^D \times N_\mathcal{F}}$

$$(\mathbb{G}_{S^m}^h)_{k\hat{\ell}(j)} = (\varphi_{i,k}^\star |_{S^m}, \varphi_{j,\ell}^\star |_{S^m}) \quad k \in \mathcal{N}_i^D, \ell \in \mathcal{N}_j^D, \quad (33)$$

198 with i and j taken from the map $I_S(m)$, $\hat{\ell}(i) = \sum_{p < i} N_p^D + \ell$ and the symbol \star shall
 199 be left empty or shall substitute with D according to the indices numbering. Thus, the
 200 discrete counterpart of problem (25) becomes find $h \in V_\delta$

$$\min_{u \in W_\delta} J_\delta(h, u) \quad \text{s.t.} \quad G_\delta(h, u) = 0. \quad (34)$$

201 Following the same approach applied for the definition of (26), this optimization dis-
 202 crete problem can be solved introducing the adjoint Lagrange multiplier $p \in V_\delta$. Ap-
 203 plying the Galerkin approach with the definition of the space $\mathcal{X}_\delta := V_\delta \times W_\delta \times V_\delta$, we ob-
 204 tain the discrete Lagrangian functional $\mathcal{L}_\delta : \mathcal{X}_\delta \rightarrow \mathbb{R}$ defined for all $w_\delta := (h, u, -p) \in$
 205 \mathcal{X}_δ as

$$\mathcal{L}_\delta(w_\delta) = J_\delta(h, u) - p^T G_\delta(h, u), \quad (35)$$

206 which leads to the following optimality system

$$\mathbb{M}_\delta w_\delta = f_\delta, \quad (36)$$

where

$$\mathbb{M}_\delta := \begin{pmatrix} \mathbb{G}^h & -\alpha \mathbb{B}^h & \mathbb{A}^T \\ -\alpha \mathbb{B}^u & \mathbb{G}^u & -\mathbb{B}^T \\ \mathbb{A} & -\mathbb{B} & 0 \end{pmatrix}, \quad f_\delta := \begin{pmatrix} 0 \\ 0 \\ q - \mathbb{A}^D h^D \end{pmatrix},$$

207 with $\mathbb{M}_\delta \in \mathbb{R}^{(2N_\tau + N^S) \times (2N_\tau + N^S)}$ and $f_\delta \in \mathbb{R}^{2N_\tau + N^S}$. The matrix \mathbb{M}_δ is symmetric and non
 208 singular, [26], and the solution of the equation (36) is the unique minimizer of (34).
 209 Due to the choice of not conformity meshes on the traces, taking a trace mesh coarser
 210 with respect to the fracture mesh, we have a non vanishing discrete inf-sup lower bound
 211 $\beta_{\delta, LB}$, with possible very small values, [13]. Thus, classical RBM a posteriori theory
 212 can be unreliable as it is well outlined in next section.

213 3.3. The Parametrized Problem

214 The optimization problem (34) and the linear system (36) are now rewritten as a
 215 parametrized problem dependent from a set of parameters $\mu = (\mu_1, \dots, \mu_P) \in \mathcal{P} \subset \mathbb{R}^P$

$$\min_{u \in W_\delta} J_\delta(h, u; \mu) \quad \text{s.t.} \quad G_\delta(h, u; \mu) = 0, \quad (37)$$

$$\mathbb{M}_\delta(\mu) w_\delta(\mu) = f_\delta(\mu). \quad (38)$$

216 The set of parameters \mathcal{P} is chosen following the model we apply to compute K_i on each
 217 fracture F_i . A common approach used in the applications, [27], is to define a three-
 218 dimensional stochastic field $\mathcal{K} : D \times \Omega \rightarrow \mathbb{R}$ and the distribution of $K_i(\omega)$ is computed
 219 as the mean value $K_i(\omega) := \frac{1}{|F_i|} \int_{F_i} \mathcal{K}(x, \omega) dx$. According to geological measurements,
 220 $\mathcal{K}(x, \omega)$ may follows the law $\mathcal{K}(x, \omega) = b^{L(x, \omega)}$, where $b > 1$ is a constant and $L : D \times$
 221 $\Omega \rightarrow \mathbb{R}$ is a stochastic field with measurable mean value $\mathbb{E}[L] : D \rightarrow \mathbb{R}$ and covariance
 222 function $C_L : D \times D \rightarrow \mathbb{R}$. Assuming C_L continuous on its domain, the Karhunen-
 223 Loève decomposition of L can be applied, see [28, 29], as follows $L(x, \omega) = \mathbb{E}[L](x) +$
 224 $\sum_{n=1}^{\infty} \sqrt{\lambda_n} \varphi_n(x) Y_n(\omega)$, where (λ_n, φ_n) is the eigenvalue-eigenvector pair of the compact
 225 operator $T\varphi = \int_D C_L(z, \cdot) \varphi(z) dz$ and Y_n are mutually uncorrelated random variables
 226 with $\mathbb{E}[Y_n] = 0$ and $\mathbb{E}[Y_n^2] = 1$. As in [29], we consider $C_L(x, z) = \exp\left(-\frac{\|x-z\|_2^2}{\gamma^2}\right)$,
 227 being γ the measure of the correlation length and Y_n uniformly distributed; hence $Y_n \sim$
 228 $\mathcal{U}(-\sqrt{3}, \sqrt{3}) = \sqrt{3}(2\tilde{Y}_n - 1)$, with $\tilde{Y}_n \sim \mathcal{U}(0, 1)$. Finally, we define $\mathcal{P} := \prod_{p=1}^P [0, 1] \subset$
 229 \mathbb{R}^P and we truncate the K.-L. series to the sum of P terms obtaining $L_P : D \times \mathcal{P} \rightarrow \mathbb{R}$
 230 defined as $L_P(x; \mu) := \mathbb{E}[L](x) + \sum_{p=1}^P \sqrt{\lambda_p} \varphi_p(x) \mu^p$.

231 Therefore, we introduce $\mathcal{K}_P(x; \mu) = b^{L_P(x; \mu)} : D \times \mathcal{P} \rightarrow \mathbb{R}$ and for each $i \in I$ the
 232 conductivity parameter map $K_{i, P} : \mathcal{P} \rightarrow \mathbb{R}$ becomes

$$K_{i, P}(\mu) := \frac{1}{|F_i|} \int_{F_i} \mathcal{K}_P(x; \mu) dx. \quad (39)$$

233 This definition allows us to show the μ -affine, or μ -separable form of the parametric lin-
 234 ear system (38): replacing the constant α introduced in (21) with a positive parametric

235 function $\alpha : \mathcal{P} \rightarrow \mathbb{R}^+$ chosen arbitrarily, we have for each $\mu \in \mathcal{P}$

$$\begin{aligned} \mathbb{M}_\delta(\mu) &= \mathbb{M}_\delta^c + \alpha(\mu)\mathbb{M}_\delta^S + (\alpha^2(\mu) + 1)\mathbb{M}_\delta^{\mathbb{G}_\mathcal{F}^h} + (\alpha^2(\mu) - 1)\mathbb{M}_\delta^{\mathbb{G}_\mathcal{S}^h} + \sum_{i \in \mathcal{I}} K_{i,\mathcal{P}}(\mu)\mathbb{M}_\delta^{\mathcal{F},i}, \\ f_\delta(\mu) &= f_\delta^c - \alpha(\mu)f_\delta^S - \sum_{i \in \mathcal{I}} K_{i,\mathcal{P}}(\mu)f_\delta^{\mathcal{F},i}. \end{aligned} \quad (40)$$

The following matrices in $\mathbb{R}^{(2N_\mathcal{F}+N^S) \times (2N_\mathcal{F}+N^S)}$ are defined as

$$\begin{aligned} \mathbb{M}_\delta^c &:= \begin{pmatrix} 0 & 0 & 0 \\ 0 & \mathbb{G}^u & -\mathcal{B}^T \\ 0 & -\mathcal{B} & 0 \end{pmatrix}, \mathbb{M}_\delta^{\mathcal{F},i} := \begin{pmatrix} 0 & 0 & \mathbb{A}_{\mathcal{F},i}^T \\ 0 & 0 & 0 \\ \mathbb{A}_{\mathcal{F},i} & 0 & 0 \end{pmatrix} \\ \mathbb{M}_\delta^S &:= \begin{pmatrix} 0 & -\mathbb{B}^h & \mathbb{A}_\mathcal{S}^T \\ -\mathbb{B}^u & 0 & 0 \\ \mathbb{A}_\mathcal{S} & 0 & 0 \end{pmatrix}, \mathbb{M}_\delta^{\mathbb{G}_\mathcal{F}^h} := \begin{pmatrix} \mathbb{G}_\mathcal{F}^h & 0 & 0 \\ 0 & 0 & 0 \\ 0 & 0 & 0 \end{pmatrix}, \mathbb{M}_\delta^{\mathbb{G}_\mathcal{S}^h} := \begin{pmatrix} \mathbb{G}_\mathcal{S}^h & 0 & 0 \\ 0 & 0 & 0 \\ 0 & 0 & 0 \end{pmatrix} \end{aligned}$$

236 and the right-hand-side vectors in $\mathbb{R}^{(2N_\mathcal{F}+N^S)}$ are defined as $f_\delta^c := (0, 0, q)^T$, $f_\delta^S :=$
 237 $(0, 0, \mathbb{A}_\mathcal{S}^D h^D)^T$ and $f_\delta^{\mathcal{F},i} := (0, 0, \mathbb{A}_{\mathcal{F},i}^D)^T$. Block-diagonal matrices $\mathbb{A}_\mathcal{S} := \text{diag}(\mathbb{A}_{\mathcal{S}_i})_{i \in \mathcal{I}} \in$
 238 $\mathbb{R}^{N_\mathcal{F} \times N_\mathcal{F}}$ and $\mathbb{A}_\mathcal{S}^D := \text{diag}(\mathbb{A}_{\mathcal{S}_i}^D)_{i \in \mathcal{I}} \in \mathbb{R}^{N_\mathcal{F} \times N_\mathcal{F}}$ are defined applying (29); similarly, matri-
 239 ces $\mathbb{A}_{\mathcal{F},i} \in \mathbb{R}^{N_\mathcal{F} \times N_\mathcal{F}}$ and $\mathbb{A}_{\mathcal{F},i}^D \in \mathbb{R}^{N_\mathcal{F} \times N_\mathcal{F}}$ are created as follow for each $i \in \mathcal{I}$

$$\mathbb{A}_{\mathcal{F},i}^\star := \begin{pmatrix} 0 & \dots & 0 \\ \vdots & \mathbb{A}_{\mathcal{F}_i}^\star & \vdots \\ 0 & \dots & 0 \end{pmatrix}, \quad (41)$$

240 in which the symbol \star shall be left empty or shall substitute with D according to the
 241 matrix to define. The matrices \mathbb{G}^u , $\mathbb{G}_\mathcal{F}^h$, $\mathbb{G}_\mathcal{S}^h$, \mathcal{B} , \mathbb{B}^h are defined in (31)-(33). Equation
 242 (40) is usually written in the classical affine compact form

$$\sum_{q=1}^{Q_M} \theta_M^q(\mu) \mathbb{M}_\delta^q w_\delta(\mu) = \sum_{q=1}^{Q_f} \theta_f^q(\mu) f_\delta^q, \quad (42)$$

243 where $Q_M = I + 4$, $Q_f = I + 2$ and $\theta_M^q, \theta_f^q : \mathcal{P} \rightarrow \mathbb{R}$ are μ -dependent functions.

244 4. The Reduction Strategy

245 For the reduction of problem (37) we consider an aggregated trial space strategy
 246 to guarantee the stability of the reduced approximation, [17, 30, 31, 1]. As before, we
 247 use the same symbol to denote both the discrete functions and the vectors of its DOFs.
 248 Choosing $N_\mu \in \mathbb{R}$, we define for each $\mu^n \in \mathcal{P}$, $n \in (1, \dots, N_\mu)$ the spaces $V_{N_\mu, p} :=$
 249 $\text{span}\{h(\mu^n), p(\mu^n)\} \subset V_\delta$ and $W_{N_\mu} := \text{span}\{u(\mu^n)\} \subset W_\delta$ of dimension $N_{h,p} = 2N_\mu$ and
 250 $N_u = N_\mu$ respectively. Space $V_{N_\mu, p}$ represents the ‘‘aggregated’’ space for the state and
 251 adjoint variables, introduced to recover the inf-sup condition of the reduced problem
 252 (4) required for the stability of the RB approximation, [31].

The reduction of equation (38) can be performed introducing the space $\mathcal{X}_N := V_{N_{h,p}} \times W_{N_u} \times V_{N_{h,p}} \subset \mathcal{X}_\delta$ of dimension $N = 2N_{h,p} + N_u$ and the matrix

$$\mathbb{V} := \text{diag}(\mathbb{V}_{h,p}, \mathbb{W}_u, \mathbb{V}_{h,p}) \in \mathbb{R}^{(2N_{\mathcal{F}} + N^S) \times N},$$

253 with $\mathbb{V}_{h,p} \in \mathbb{R}^{N_{\mathcal{F}} \times N_{h,p}}$ the column-wise collection of $\{\zeta_n\}_{n \in \{1, \dots, N_{h,p}\}}$ orthonormal basis of
 254 $V_{N_{h,p}}$ and $\mathbb{W}_u \in \mathbb{R}^{N^S \times N_u}$ the column-wise collection of $\{\xi_n\}_{n \in \{1, \dots, N_u\}}$ orthonormal basis
 255 of W_{N_u} . Calling $w_N := (h_N, u_N, p_N) \in \mathcal{X}_N$ we obtain the reduced problem

$$\mathbb{V}^T \mathbb{M}_\delta(\mu) \mathbb{V} w_N(\mu) = \mathbb{V}^T f_\delta(\mu) \Leftrightarrow \mathbb{M}_N(\mu) w_N(\mu) = f_N(\mu) \quad (43)$$

256 in which we apply the Galerkin-RB approximation hypothesis, see [17] for further
 257 details. In conclusion, having defined a classical RB projection base on space \mathcal{X}_N , the
 258 whole RB methodology is available, such as POD or greedy algorithms for the selection
 259 of the RB-basis \mathbb{V} . Moreover, the affine parametric dependence of the operators, proved
 260 in (42), allows us to use the offline / online decomposition in order to obtain the solution
 261 of the problem.

262 4.1. DFN Error Estimates

263 We introduce the matrix $\mathbb{X}_\delta \in \mathbb{R}^{(2N_{\mathcal{F}} + N^S) \times (2N_{\mathcal{F}} + N^S)}$ to compute, given $w_\delta = (h, u, p) \in$
 264 \mathcal{X}_δ the norm

$$\begin{aligned} \|w_\delta\|_{\mathbb{X}_\delta}^2 &:= w_\delta^T \mathbb{X}_\delta w_\delta = \sum_{i \in \mathcal{I}} |h_i|_{H^1(F_i)}^2 + |p_i|_{H^1(F_i)}^2 + \\ &\sum_{S^m \in \mathcal{S}_i} \left(\|h_i|_{S^m}\|_{L^2(S^m)}^2 + \|p_i|_{S^m}\|_{L^2(S^m)}^2 + \|u_i^m\|_{H^{-1/2}(S^m)}^2 \right) \end{aligned} \quad (44)$$

265 in which $\|\cdot\|_{H^{-1/2}(S^m)} : W_{\delta,i}^m \rightarrow \mathbb{R}$ is approximated by $\|u_i^m\|_{H^{-1/2}(S^m)}^2 = \sum_{\lambda \in \mathcal{T}_i^m} |\lambda| \|u_i^m\|_{L^2(\lambda)}^2$,
 266 with λ the element of the mesh \mathcal{T}_i^m chosen on S^m in F_i . Recalling $K_{i,\mathcal{P}}$ in defini-
 267 tion (39) and choosing $\alpha^2(\mu) = \overline{K_{i,\mathcal{P}}(\mu)} = I^{-1} \sum_{i \in \mathcal{I}} K_{i,\mathcal{P}}$ in (28), it is possible to show
 268 that $\|w_\delta\|_{\mathbb{X}_\delta} \approx \alpha(\mu) \|\hat{w}_\delta\|_{\mathbb{X}_\delta}$, being $\hat{w}_\delta = (h, \alpha(\mu)^{-1}u, p)$. The residual R_δ introduced
 269 in (8) becomes for the DFN optimization problem $R_\delta(w_\delta; \mu) = \mathbb{M}_\delta(\mu) w_\delta(\mu) - f_\delta(\mu)$
 270 and the the inf-sup constant $\beta_\delta(\mu)$ defined in (6) is computed in the discrete opti-
 271 mization problem (37) as the smallest singular value $\sigma_{\min}(\mathbb{X}_\delta^{-\frac{1}{2}} \mathbb{M}_\delta(\mu) \mathbb{X}_\delta^{\frac{1}{2}})$. Finally,
 272 we introduce the a posteriori error estimator $\Delta_\delta(\cdot; \mu)$ involved in (13) for problem
 273 (37) as in [15]. Let T and e the elements and the edges of mesh \mathcal{T}_i on fracture F_i ,
 274 $\eta_{H,i}^2 := \sum_T \frac{|T|^2}{K_{i,\mathcal{P}}} \|q_i + K_{i,\mathcal{P}} \Delta h_i\|_{L^2(T)}^2$ the residual estimator of the Darcy's equation and
 275 $\eta_{P,i}^2 := \sum_T K_{i,\mathcal{P}} |p_i|_{H^1(T)}^2$ the estimator of the discontinuity of h between the fractures.
 276 Moreover, we introduce $\xi_{U,i}^2 := \sum_e \frac{|e|}{K_{i,\mathcal{P}}} \left\| \left[\frac{\partial h_i}{\partial \nu^m} \right] - \tilde{u}_i \right\|_{L^2(e)}^2$ the estimator for the approxi-
 277 mation of the flux through the edges of the mesh, where $\tilde{u}_i := u_i^m - \alpha h_i|_{S^m}$ is non-zero
 278 only on $e \cap S^m \neq \emptyset, \forall S^m \in \mathcal{S}_i$. Similarly, being \mathcal{T}_i^m the mesh of elements λ on
 279 each trace $S^m \in \mathcal{S}_i$, we denote by $\xi_{NC,m}^2 := \sum_\lambda \frac{|\lambda|}{K_{i,\mathcal{P}}} \|u_i^m - \alpha h_i|_{S^m}\|_{L^2(\lambda)}^2$ the estimator for

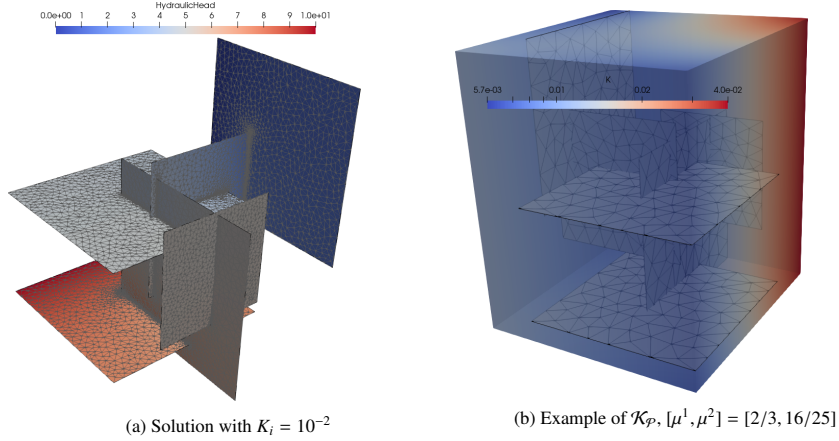


Figure 2: FracTest - Overview

(a) Problem size

ε_δ	$N_{\mathcal{F}}$	N^S
10^{-1}	2,043	376
$5 \cdot 10^{-2}$	18,557	1,920

(b) Convergences Rates $\nu e^{-\rho N}$

Test	ε_δ	ν	ρ
$\Delta_{\delta, N}$	10^{-1}	$1.9133 \cdot 10^{-1}$	$1.2675 \cdot 10^{-1}$
Δ_N	10^{-1}	$1.3871 \cdot 10^{-1}$	$1.2847 \cdot 10^{-1}$
$\Delta_{\delta, N}$	$5 \cdot 10^{-2}$	$1.7179 \cdot 10^{-1}$	$1.1834 \cdot 10^{-1}$
Δ_N	$5 \cdot 10^{-2}$	$5.8893 \cdot 10^{-2}$	$1.1748 \cdot 10^{-1}$

Table 1: Frac6 - Data

280 the non-conformity of the discretization, by $\xi_{P,m}^2 := \sum_\lambda \frac{|\lambda|}{K_{i,\mathcal{F}}} \|p_i|_{S^m}\|_{L^2(\lambda)}^2$ the estimator
 281 for the hydraulic head induced by the unbalancing of fluxes on the mesh and by $J_m^2 :=$
 282 $\sum_\lambda \frac{|\lambda|(1+\alpha)^2}{\min(K_{i,\mathcal{F}}, K_{j,\mathcal{F}})} \|u_i^m + u_j^m - \alpha(h_i|_{S^m} + h_j|_{S^m})\|_{L^2(\lambda)}^2 + \sum_\lambda \frac{|\lambda|}{\min(K_{i,\mathcal{F}}, K_{j,\mathcal{F}})} \|h_i|_{S^m} - h_j|_{S^m}\|_{L^2(\lambda)}^2$ the
 283 estimator of the functional minimization error. Collecting all the definitions the esti-
 284 mator turns out to be $\forall \mu \in \mathcal{P}$

$$\Delta_\delta^2(w_\delta; \mu) := \sum_{i \in \mathcal{I}} \left(\eta_{H,i}^2 + \eta_{P,i}^2 + \xi_{U,i}^2 + \sum_{S^m \in \mathcal{S}_i} \left(\xi_{NC,m}^2 + \xi_{P,m}^2 + J_m^2 \right) \right). \quad (45)$$

285 For the proof of (13) and further details of the definition of the quantities in (45) see
 286 [15, 22].

287 5. Numerical Results

288 For two different DFNs with growing complexity we perform the comparison of
 289 our estimator (Algorithm 2) with the classical greedy interpolation strategy proposed
 290 in [18] (Algorithm 1). Then, the RB certification is measured through the statistical

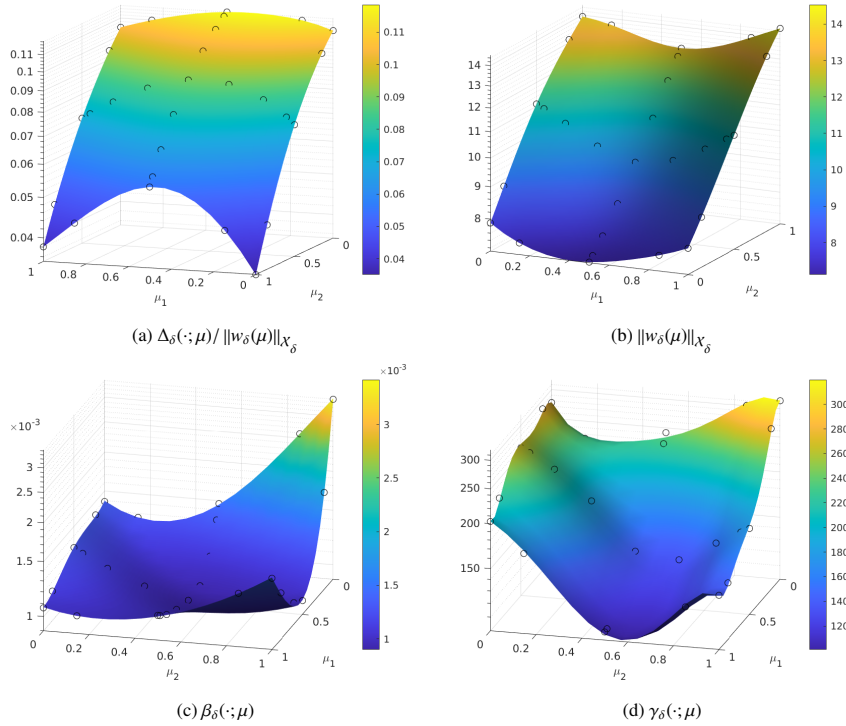


Figure 3: Frac6 - Interpolation with $\mathcal{P} = 2$, $I_\ell = 3$, $\varepsilon_\delta = 10^{-1}$. Black dots represent the sparse interpolation grid

291 analysis of the error $e_{\delta, N}$ on a random set of parameters $S_{\text{Test}} \subset \mathcal{P}$. The numerical tests
 292 are performed with relatively small DFNs because we focus on the validation of the
 293 proposed algorithm rather than on an efficient and robust implementation. The simula-
 294 tions for the resolution of the high-fidelity model are performed with the C++ software
 295 introduced in [12] applied to the optimization method of Section 3 and restricted to the
 296 serial case [32]. The post-processing analysis for the RBM theory provided in Section 4
 297 is implemented in the MATLAB software.

298 5.1. Test 1 - DFN simple problem

299 The first test is performed on a simple problem called *Frac6*, with $I = 6$ and $M = 6$.
 300 Figure 2a shows the geometry of the network and an example of the solution of the dis-
 301 crete problem (37) computed with $K_i = 10^{-2}$ for all $i \in \mathcal{I}$ on an adaptive mesh. Two
 302 Dirichlet boundary conditions are imposed, namely a value of 10 in the bottom left
 303 fracture and a value of zero on the top right fracture; zero Neumann boundary condi-
 304 tions are required on the other borders and no forcing term is applied on each fracture.
 305 Figure 2b shows an example of the conductivity field $\mathcal{K}_\mathcal{P}$ with the DFN immersed;
 306 both the example and the following numerical tests are performed using \mathcal{P} of dimen-
 307 sion $\mathcal{P} = 2$ and taking the parameters of Conductivity field described in Section 4

308 equal to $\gamma = 0.25$, $\mathbb{E}[L] = -2$ and $b = 10$, that can be realistic values as already stated
 309 in [29]. The two meshes used to solve the high fidelity problem are chosen by the
 310 adaptive method described in [22] and are kept fixed independent of the dimension N
 311 of the space \mathcal{X}_N . The adapted meshes are obtained solving the optimization problem
 312 with parameter $K_i = b^{\mathbb{E}[L]} = 10^{-2} \forall i \in \mathcal{I}$, performing few adaptive iterations starting
 313 from a mesh with 100 DOFs and imposing two different values of the tolerance ε_δ (16)
 314 equal to 10^{-1} and 10^{-2} . Table 1a shows the resulting size of the discrete problem in
 315 both the tests. Figures 3 and 4 show the interpolation of all the quantities used in the
 316 RBM offline computations in both the tests; the surfaces are generated starting from
 317 a Smolyak's sparse grid [33] of level $I_\ell = 3$, to mitigate the curse of dimensionality
 318 problem with higher \mathcal{P} . A radial basis functions (RBF) interpolations of degree 5 of the
 319 relative a posteriori error $\Delta_\delta(\cdot; \mu) / \|w_\delta(\mu)\|_{\mathcal{X}_\delta}$ and of the norm $\|w_\delta(\mu)\|_{\mathcal{X}_\delta}$ are represented
 320 in Figures 3a-4a and in Figures 3b-4b. Finally, the discrete inf-sup constant $\beta_\delta(\cdot; \mu)$ and
 321 the discrete continuity constant $\gamma_\delta(\cdot; \mu)$ are approximated with a least squares approxi-
 322 mation of degree 5 and reported in Figures 3c-3d and Figures 4c-4d. The computation
 323 of the $\beta_\delta(\cdot; \mu)$ and $\gamma_\delta(\cdot; \mu)$ values in the interpolation points are performed as described
 324 in Section 4.1. Comparing Figure 3c and Figure 4c we can notice that the shape of the
 325 surfaces seems not to be influenced by the mesh size. Moreover, recalling (9), we can
 326 see that the effectivity index $\eta_\delta(\cdot; \mu)$ on the domain \mathcal{P} in both cases is bounded by an
 327 average condition number $\kappa_\delta(\cdot; \mu)$ in the order of 10^5 ; this means that, even in this small
 328 and simple DFN, the classic RBM estimation $\Delta_N(\cdot, \mu)$ can be quite inaccurate. Figure 6
 329 shows the convergences of both the greedy Algorithms 1 and 2 in which we impose
 330 $\varepsilon_N = 10^{-8}$ and $M = 100$. Although not required, in Algorithm 2, we compute also
 331 the classical RBM estimator $\Delta_N(\cdot; \mu)$ for comparison reasons. Figure 5a shows the set
 332 S_M used as input of both the algorithms and generated by a classic uniform tensorial
 333 \mathcal{P} -grid generated from a 1D-Chebyshev grid of size 10. Focusing on the convergence
 334 obtained, by comparing Figure 6a and Figure 6b we can say again that the mesh size
 335 does not have relevant impacts on the convergence rate of the RB error $e_{\delta,N}(\cdot; \mu)$ in both
 336 the greedy algorithms. Moreover, the curves $\max_{\mu \in S_M} \Delta_N / \|w_N\|_{\mathcal{X}_\delta}$ in Figure 6
 337 by the two algorithms are almost overlapped, but the error estimator $|\Delta_{\delta,N} - \Delta_{\delta,I}| / \Delta_{\delta,I}$
 338 seems not strongly influenced by the high condition number $\kappa_\delta(\cdot; \mu)$. Therefore, the
 339 two algorithms are performing the choice of the reduced basis in a similar way, but
 340 Algorithm 2 relies on a more sharp stopping criterion. As suggested in Section 2 from
 341 the triangle inequality (16), we set $\varepsilon_N \lesssim \varepsilon_\delta$ in order to stop the greedy Algorithm 2
 342 as soon as possible without any loss of accuracy. In particular, the first test with
 343 $\varepsilon_N \lesssim \varepsilon_\delta = 10^{-1}$ comes to a good approximation with N between 10 and 20 and the
 344 second case with $\varepsilon_N \lesssim \varepsilon_\delta = 10^{-2}$ seems have an optimal stop at N between 20 and
 345 40. In Figure 7 we report the dimension N for different ε_N reached by Algorithm 1 and
 346 Algorithm 2 for the two considered values of ε_δ ; the plots confirm the effectiveness of
 347 Algorithm 2.

348 To validate the results of the greedy algorithms, we use the RBM space \mathcal{X}_N obtained
 349 to compare the online solution with the corresponding high fidelity solution on a trial
 350 set $S_{\text{Test}} \subseteq [0, 1]^2$ (see Figure 5b) of size $|S_{\text{Test}}| = 100$ randomly generated with uniform
 351 distribution. Figure 8 shows for each ε_δ the real relative RB error $\|e_{\delta,N}\|_{\mathcal{X}_\delta} / \|w_N\|_{\mathcal{X}_\delta}$
 352 computed for each $\mu_{\text{Test}} \in S_{\text{Test}}$ on two N ; we measure all the quantities used inside the

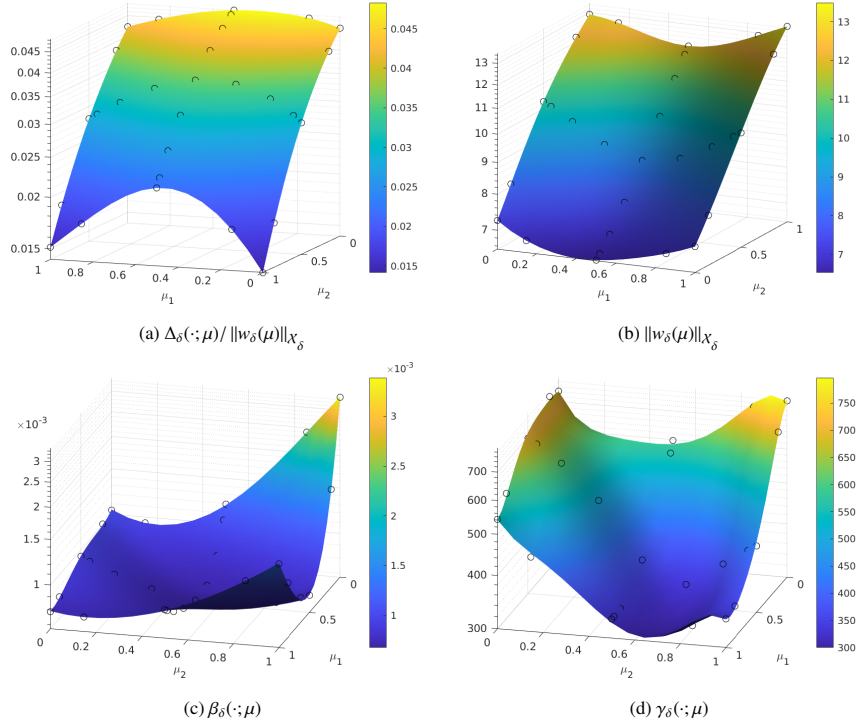


Figure 4: Frac6 - Interpolation with $\mathcal{P} = 2$, $I_\ell = 3$, $\varepsilon_\delta = 5 \cdot 10^{-2}$. Black dots represent the sparse interpolation grid

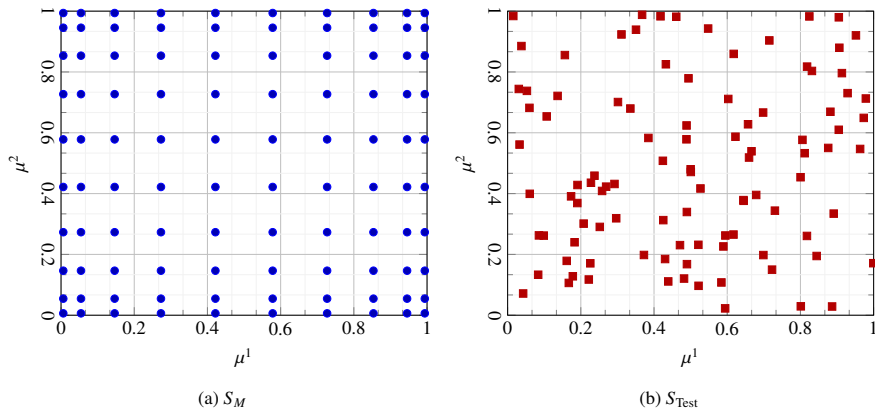


Figure 5: Greedy Offline/Online set - \mathcal{P} of dimension $\mathcal{P} = 2$

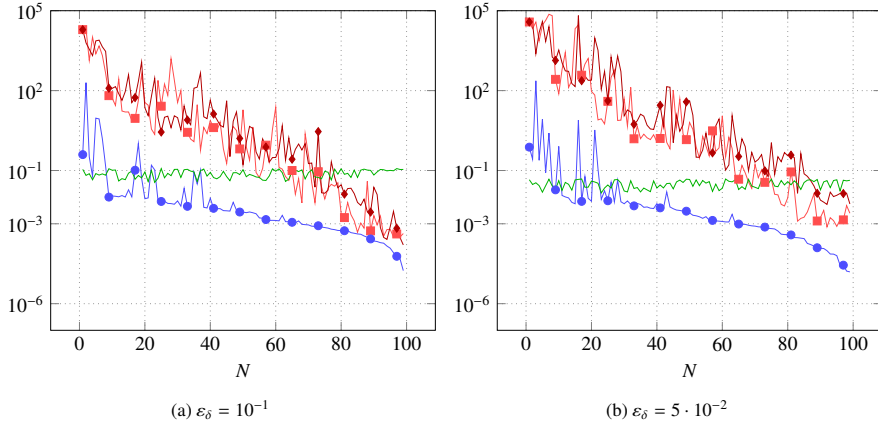


Figure 6: Convergence of Algorithm 1 and Algorithm 2 applied to Frac6. Legend: \blacksquare Algorithm 1 $\max_{\mu \in S_M} \Delta_N / \|w_N\|_{\chi_\delta}$, \bullet Algorithm 2 $\max_{\mu \in S_M} \Delta_N / \|w_N\|_{\chi_\delta}$, \bullet $\max_{\mu \in S_M} |\Delta_{\delta,N} - \Delta_{\delta,I}| / \Delta_{\delta,I}$, \bullet $\max_{\mu \in S_M} \Delta_{\delta,I} / \|w_{\delta,I}\|_{\chi_\delta}$

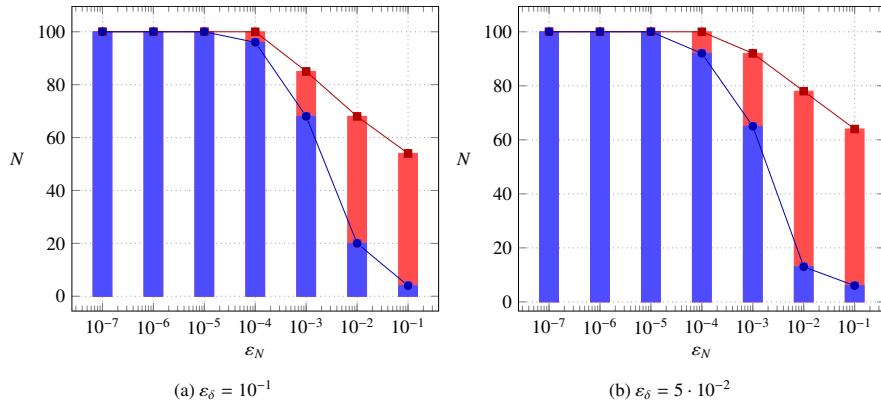


Figure 7: Frac6 - Legend: \blacksquare Convergence of Algorithm 1, \bullet Convergence of Algorithm 2

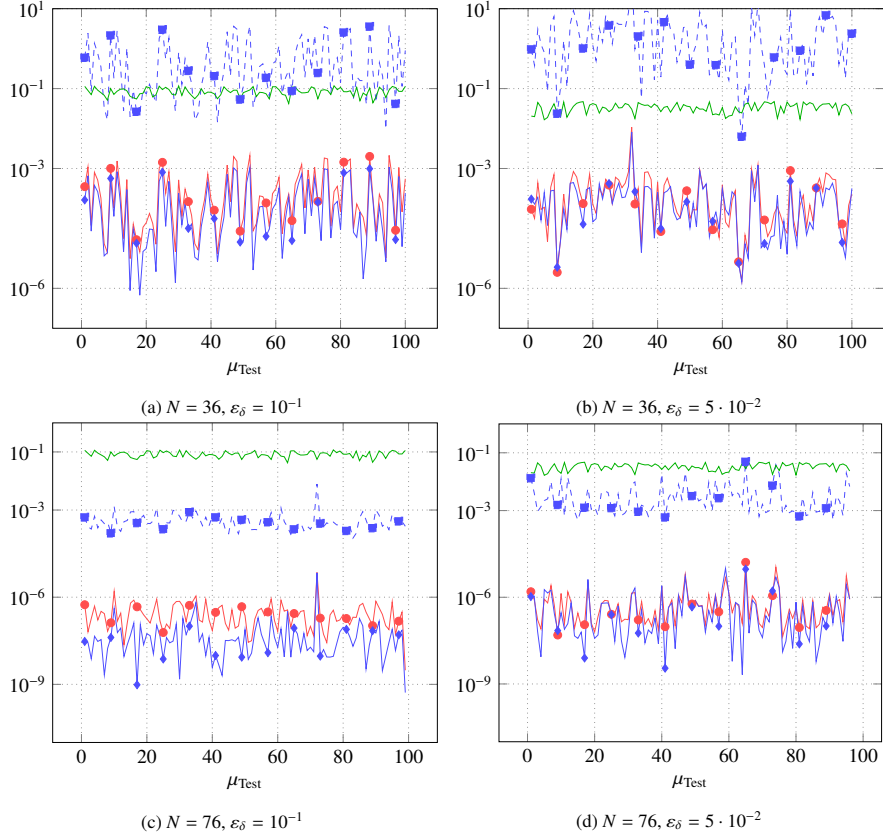


Figure 8: Frac6 - RBM Online, $|S_{\text{Test}}| = 100$. Legend: \square $\Delta_N / \|w_N\|_{\mathcal{X}_\delta}$, \bullet $\|e_{\delta,N}\|_{\mathcal{X}_\delta} / \|w_N\|_{\mathcal{X}_\delta}$, \blacklozenge $|\Delta_{\delta,N} - \Delta_{\delta,I}| / \Delta_{\delta,I}$, --- $\Delta_{\delta,I} / \|w_{\delta,I}\|_{\mathcal{X}_\delta}$

353 greedy algorithms in order to compare the ability of the estimators to tackle the real
 354 error $e_{\delta,N}$. Relative estimator $\Delta_{\delta,I} / \|w_{\delta,I}\|_{\mathcal{X}_\delta}$ of error e_δ is also reported as a reference
 355 value for comparisons. As we expect, from the plots we can see that the relative classic
 356 RBM estimation $\Delta_N(\cdot; \mu)$ is far from the relative error even in this small case; on the
 357 other hand the new estimator proposed seems to be very close to the value expected.
 358 We shall remark that the estimator is not completely above or under the RBM error as
 359 we neglect the constants C_* and C^* in (15). From the very small distance between the
 360 curves we see in the plots, we can say that this assumption seems appropriate.

361 Figure 9 reports the average relative RBM error $\|e_{\delta,N}\|_{\mathcal{X}_\delta} / \|w_N\|_{\mathcal{X}_\delta}$ measured on the
 362 RBM online tests at different RB space size N , with its standard deviations; classic
 363 RBM estimator is also reported. Notice how the curve of the a posteriori error $\Delta_{\delta,I}$
 364 related to the RB solution norm $\|w_N\|_{\mathcal{X}_\delta}$ becomes constant increasing N , thanks to the
 365 convergence of the RB solution to the discrete one w_δ . We can say that the results
 366 obtained on the trial set are compliant to the one depicted in Figure 7 in all the tests

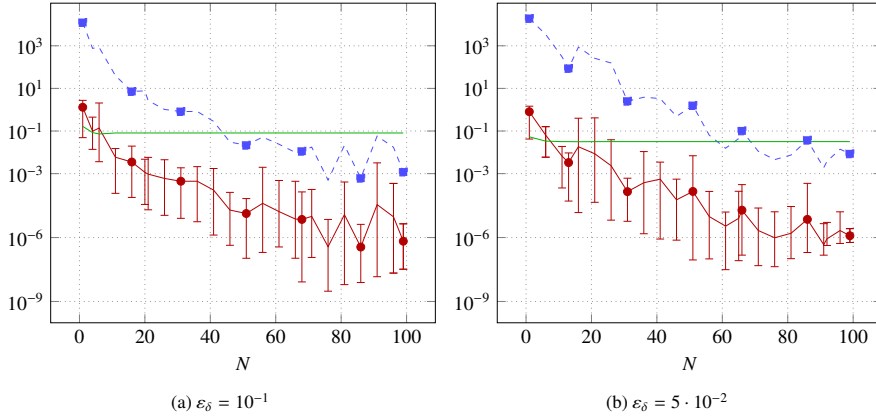


Figure 9: Frac6 - RBM Online, $|S_{\text{Test}}| = 100$. Legend: \bullet avg $\|e_{\delta,N}\|_{\mathcal{X}_\delta} / \|w_N\|_{\mathcal{X}_\delta}$, \blacksquare avg $\Delta_N / \|w_N\|_{\mathcal{X}_\delta}$, --- avg $\Delta_{\delta,N} / \|w_N\|_{\mathcal{X}_\delta}$

367 performed. Moreover, the plots corroborate that no relevant differences can be observed
 368 comparing the coarse mesh with respect to the finer one. To conclude the analysis, we
 369 report in Figure 10 and in Table 1b the convergence rates computed on the RBM error
 370 $\|e_{\delta,N}\|_{\mathcal{X}_\delta}$ obtained on the trial set S_{Test} ; we remark that the symbol Δ_N identifies the
 371 estimator of Algorithm 1, whereas $\Delta_{\delta,N}$ identifies the estimator of Algorithm 2. We can
 372 see that an exponential convergence $\nu e^{-\rho N}$ typical of the Kolmogorov N -width decay of
 373 the elliptic equations is obtained also with the Algorithm 2. Finally, from Table 1b we
 374 can assert the rate of convergence ρ in the classical algorithm and in the new algorithm
 375 are comparable.

376 5.2. Test 2 - Real DFN

377 The second test is performed on an higher complexity stochastically generated
 378 DFN, called *Frac20*, with $I = 20$ and $M = 28$. The network is created with random
 379 probability distribution functions concerning size, position and orientation of fractures
 380 taken from the real data available in [34]. Even with a small number of fractures, in
 381 Figures 11a-11c we can appreciate the complexity of the geometry from three different
 382 point of view and an example of the solution of the discrete problem (37) computed
 383 through the model proposed with $K_i = 10^{-2}$ for all $i \in \mathcal{I}$. Focusing on Figure 11b, we
 384 impose a Dirichlet boundary condition of value 1 on the left side of the network and of
 385 value zero on the right part; always zero Neumann conditions are imposed on the other
 386 borders and no forcing term is present. As for the Frac6 test, Figure 11d shows a sample
 387 of the conductivity field $\mathcal{K}_\mathcal{P}$ with the DFN immersed; we keep the same parameter
 388 for the stochastic generation, therefore we use $\mathcal{P} = 2$, $\gamma = 0.25$, $\mathbb{E}[L] = -2$ and $b = 10$.
 389 We use a fixed adaptive mesh generated in the previous examples with $\varepsilon_\delta = 10^{-3}$ and
 390 Table 2a shows the resulting size of the discrete problem. From Figures 11 we can ap-
 391 preciate how the adaptive non-conforming method increases the number of mesh cells
 392 around the traces.

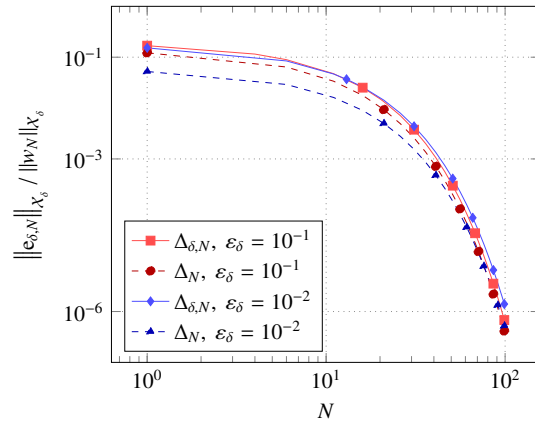


Figure 10: Frac6 - Convergences Curves $\nu e^{-\rho N}$

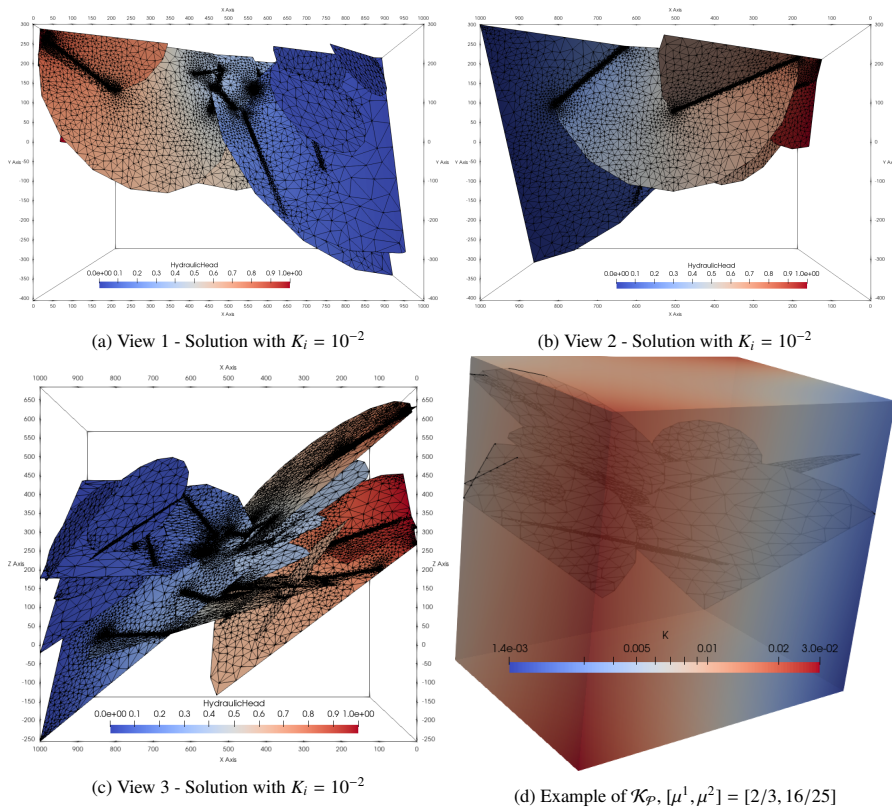


Figure 11: Frac20 - Overview

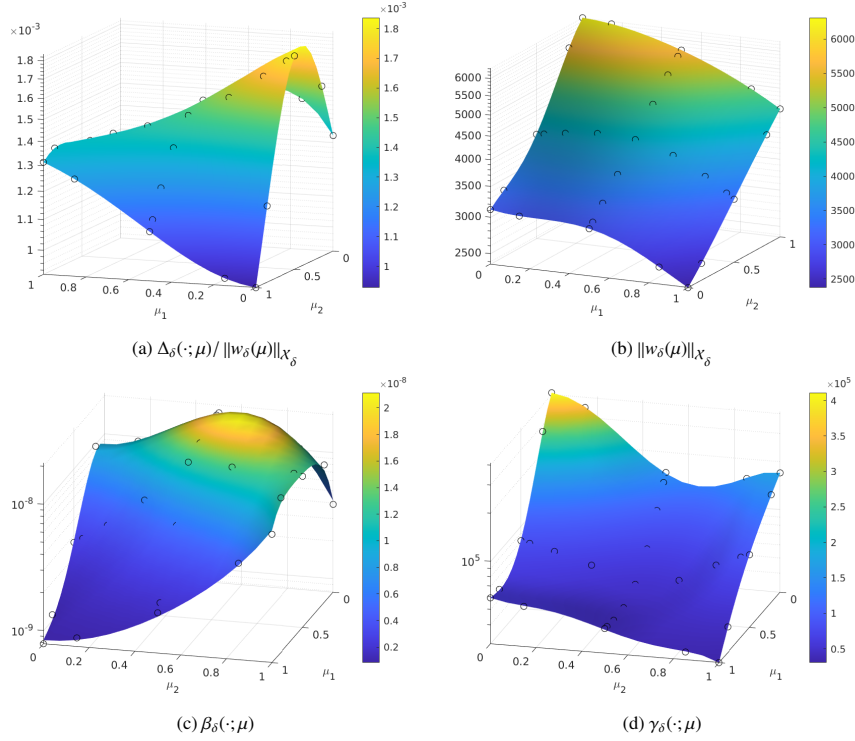


Figure 12: Frac20 - Interpolation with $\mathcal{P} = 2$, $I_\ell = 3$, $\varepsilon_\delta = 10^{-3}$. Black dots represent the sparse interpolation grid

393 Figure 12 shows the interpolation of all the quantities used in the RBM offline computations; again, a Smolyak's sparse grid quadrature rule of level $I_\ell = 3$ is used. RBF
394 interpolation of degree 5 generates Figure 12a and Figure 12b; least squares approximation of degree 5 is used for Figure 12c and Figure 12d. Comparing Figures 12a-12d
395 to Figures 3a-3d or to Figures 4a-4d it is possible to observe that each DFN has its own dependency from the parameter set \mathcal{P} . Moreover, recalling (9), we can see that
396 the average $\kappa_\delta(\cdot; \mu)$ is above 10^{13} , therefore we expect the classical RBM estimator
397 Δ_N to be not reliable. Plots in Figure 13 shows the convergence of Algorithm 1 and
398 Algorithm 2 obtained with $\varepsilon_N = 10^{-8}$ and $M = 100$. The classical RBM estimator
399 $\Delta_N(\cdot; \mu)$ is reported for both the algorithms. As expected the classic RB estimator does
400 not provide reliable information for stopping the iterations, on the other hand the new
401 estimator seems to be effective. Moreover, Figure 13b clearly shows the effectiveness
402 of Algorithm 2 to produce the RB space with a small value of N . In addition, in Fig-
403 ure 13a we observe a similar rate of convergence for the quantity $\Delta_N(\cdot; \mu)$. Taking
404 $\varepsilon_N \lesssim \varepsilon_\delta = 10^{-3}$ to stop the greedy Algorithm 2 we can say that an acceptable con-
405 vergence of the algorithm is performed with N between 60 and 80. To confirm these
406 statements, we test the RBM space \mathcal{X}_N obtained as done for the Frac6 test, evaluating
407 the online solution on a trial set $\mathcal{S}_{\text{Test}} \subseteq [0, 1]^2$ of size $|\mathcal{S}_{\text{Test}}| = 100$ randomly generated.
408
409
410

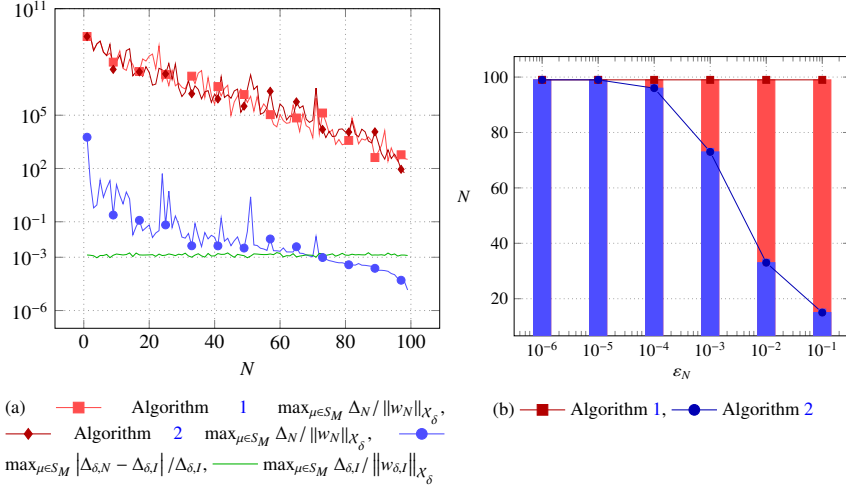


Figure 13: Convergence of Algorithm 1 and Algorithm 2 applied to Frac20, $\varepsilon_\delta = 10^{-3}$

(a) Problem size			(b) Convergences Rates $\nu e^{-\rho N}$			
ε_δ	$N_{\mathcal{F}}$	N^S	Test	ε_δ	ν	ρ
10^{-3}	25,880	2,922	$\Delta_{\delta,N}$	10^{-3}	$1.4598 \cdot 10^2$	$1.1664 \cdot 10^{-1}$
			Δ_N	10^{-3}	$1.4612 \cdot 10^2$	$1.1267 \cdot 10^{-1}$

Table 2: Frac20 - Data

411 Figure 14 displays all the quantities measured for each $\mu_{\text{Test}} \in S_{\text{Test}}$ on two N , including
412 the real distance between the RBM solution and the discrete one $\|e_{\delta,N}\|_{\mathcal{X}_\delta} / \|w_N\|_{\mathcal{X}_\delta}$. The
413 relative classic RBM $\Delta_N(\cdot; \mu)$ is far from the error, on the other hand the alternative es-
414 timator proposed is very close to the real error values. Again, the assumption to neglect
415 the constants C_* and C^* is still reliable, as the estimator $|\Delta_{\delta,N} - \Delta_{\delta,I}| / \Delta_{\delta,I}$ is of the same
416 size as the relative error $\|e_{\delta,N}\|_{\mathcal{X}_\delta} / \|w_N\|_{\mathcal{X}_\delta}$. To conclude the analysis, in Figure 15 we
417 can see how the convergence rate of the average RB error $e_{\delta,N}(\cdot; \mu)$ measured matches
418 with the values obtained in Figure 13b; again, the curve related to the DFN a posteri-
419 ori estimator $\Delta_{\delta,N}(\cdot; \mu)$ becomes constant when N grows, thanks to the convergence of
420 the RB solution w_N to the high fidelity one w_δ . Figure 15b and Table 2b confirm the
421 exponential convergences $\nu e^{-\rho N}$ of the greedy method also with the stochastic DFN.
422 We conclude the numerical tests reporting in Figure 16 two examples of the solution
423 obtained with the RBM algorithm.

424 6. Conclusion

425 A simple and robust RBM greedy approach is proposed for the creation of a re-
426 duced basis space to approximate both the hydraulic head and the flux distribution on

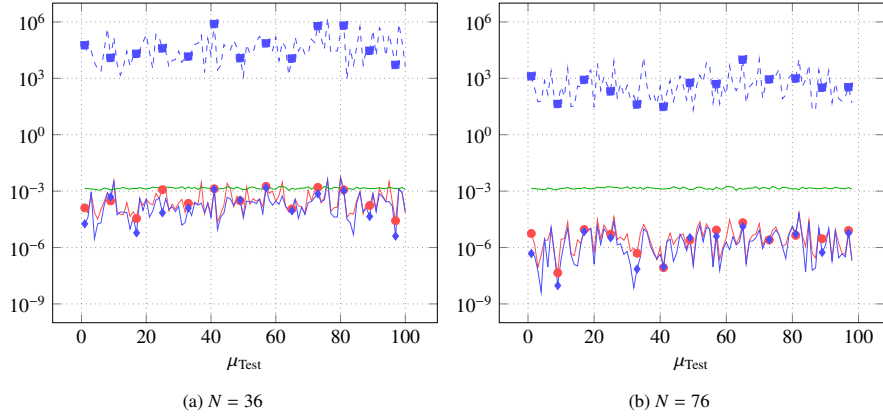


Figure 14: Frac20 - RBM Online, $|S_{\text{Test}}| = 100$, $\varepsilon_\delta = 10^{-3}$. Legend: \blacksquare $\Delta_N / \|w_N\|_{X_\delta}$, \bullet $\|e_{\delta,N}\|_{X_\delta} / \|w_N\|_{X_\delta}$, \blacklozenge $|\Delta_{\delta,N} - \Delta_{\delta,I}| / \Delta_{\delta,I}$, --- $\Delta_{\delta,I} / \|w_{\delta,I}\|_{X_\delta}$

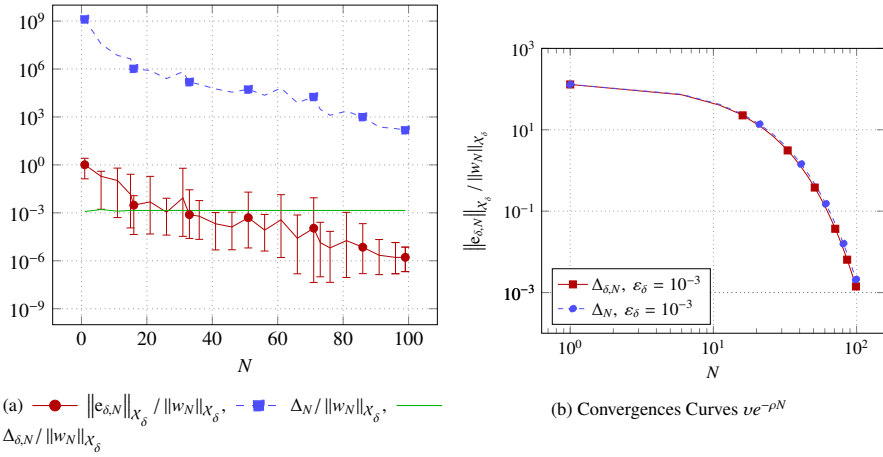


Figure 15: Frac20 - Test of RBM Online, $|S_{\text{Test}}| = 100$, $\varepsilon_\delta = 10^{-3}$

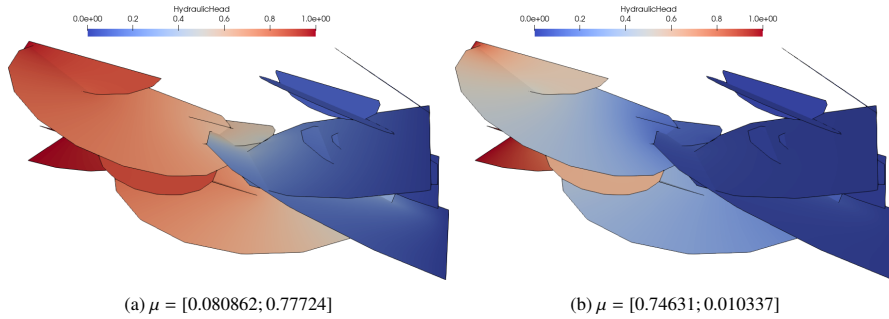


Figure 16: Frac20 - Solutions obtained with RBM

427 stochastic Discrete Fracture Networks. A smart stopping criterion for the greedy ap-
428 proach is also suggested to control the RBM space dimension taking the tolerance of
429 the greedy algorithm in the same order of magnitude of the tolerance used for the a
430 posteriori error estimate of the high fidelity solution. The algorithm relies on the a pos-
431 teriori error estimation performed on the PDE-constrained optimization problem and it
432 can be extended to a more fast and scalable solution by exploiting the parallel nature
433 of non conforming mesh on each fracture of the network. Numerical tests verify the
434 lower reliability of the classical RB a posteriori analysis and establish the validity of
435 the alternative estimator showing the equivalence of the convergence rates compared
436 to the classical RB methods.

437 **References**

- 438 [1] J. S. Hesthaven, G. Rozza, B. Stamm, *Certified Reduced Basis Methods for*
439 *Parametrized Partial Differential Equations*, Springer, 2016.
- 440 [2] S. Hain, M. Ohlberger, Radic, K. Urban, A hierarchical a posteriori error estima-
441 tor for the reduced basis method, *Advances in Computational Mathematics* 45 (5)
442 (2019) 1572–9044.
- 443 [3] M. Ali, K. Steih, K. Urban, Reduced basis methods with adaptive snapshot com-
444 putations, *Advances in Computational Mathematics* 43 (2) (2017) 257–294.
- 445 [4] J. D. Hyman, C. W. Gable, S. L. Painter, N. Makedonska, Conforming delaunay
446 triangulation of stochastically generated three dimensional discrete fracture net-
447 works: A feature rejection algorithm for meshing strategy, *SISC* 36 (4) (2014)
448 A1871–A1894.
- 449 [5] J. Hyman, S. Karra, N. Makedonska, C. Gable, S. Painter, H. Viswanathan, dfn-
450 works: A discrete fracture network framework for modeling subsurface flow and
451 transport, *Computers & Geosciences* 84 (2015) 10 – 19.
- 452 [6] H. Mustapha, K. Mustapha, A new approach to simulating flow in discrete frac-
453 ture networks with an optimized mesh, *SISC* 29 (4) (2007) 1439–1459.
- 454 [7] A. Fumagalli, A. Scotti, An efficient xfem approximation of darcy flows in arbi-
455 trarily fractured porous media, *Oil Gas Sci. Technol. – Rev. IFP Energies nou-*
456 *velles* 69 (4) (2014) 555–564.
- 457 [8] P. F. Antonietti, L. Formaggia, A. Scotti, M. Verani, N. Verzott, Mimetic finite
458 difference approximation of flows in fractured porous media, *ESAIM: M2AN*
459 50 (3) (2016) 809–832.
- 460 [9] G. Pichot, J. Erhel, J. de Dreuzy, A generalized mixed hybrid mortar method for
461 solving flow in stochastic discrete fracture networks, *SISC* 34 (2012) B86 – B105.
- 462 [10] G. Pichot, J. Erhel, J. de Dreuzy, A mortar bdd method for solving flow in stochas-
463 tic discrete fracture networks, *Domain Decomposition Methods in Science and*
464 *Engineering XXI* 98 (2014) 99 – 112.

- 465 [11] S. Berrone, S. Pieraccini, S. Scialò, A pde-constrained optimization formulation
466 for discrete fracture network flows, *SISC* 35 (2) (2013) 487–510.
- 467 [12] S. Berrone, S. Scialò, F. Vicini, Parallel meshing, discretization, and computation
468 of flow in massive discrete fracture networks, *SISC* 41 (4) (2019) 317–338.
- 469 [13] V. Girault, R. Glowinski, Error analysis of a fictitious domain method applied to a
470 dirichlet problem, *Japan Journal of Industrial and Applied Mathematics* 487 (12)
471 (1995) 317–338.
- 472 [14] S. Berrone, A. Borio, A residual a posteriori error estimate for the virtual element
473 method, *Mathematical Models and Methods in Applied Sciences* 27 (08) (2017)
474 1423–1458.
- 475 [15] S. Berrone, S. Scialò, A. Borio, A posteriori error estimate for a PDE-constrained
476 optimization formulation for the flow in DFNs, *SIAM J. Numer. Anal.* 54 (1)
477 (2016) 242–261.
- 478 [16] G. Rozza, D. B. P. Huynh, A. Patera, Reduced basis approximation and a posteri-
479 ori error estimation for affinely parametrized elliptic coercive partial differential
480 equations, *Archives of Computational Methods in Engineering* 229 (15) (2008)
481 1886–1784.
- 482 [17] A. Quarteroni, A. Manzoni, F. Negri, *Reduced Basis Methods for Partial Differ-
483 ential Equations An Introduction*, Springer, 2016.
- 484 [18] A. Manzoni, Negri, Heuristic strategies for the approximation of stability factors
485 in quadratically nonlinear parametrized pdes, *Advances in Computational Math-
486 ematics* 41 (5) (2015) 1572–9044.
- 487 [19] D. Huynh, G. Rozza, S. Sen, A. Patera, A successive constraint linear optimiza-
488 tion method for lower bounds of parametric coercivity and inf-sup stability con-
489 stants, *Comptes Rendus Mathematique* 345 (8) (2007) 473–478.
- 490 [20] M. Yano, A reduced basis method with exact-solution certificates for symmetric
491 coercive equations, *CMAME* 287 (2015) 290–309.
- 492 [21] R. Verfürth, A posteriori error estimation and adaptive mesh-refinement tech-
493 niques, *Journal of Computational and Applied Mathematics* 50 (1) (1994) 67 –
494 83.
- 495 [22] S. Berrone, A. Borio, F. Vicini, Reliable a posteriori mesh adaptivity in discrete
496 fracture network flow simulations, *CMAME* 354 (2019) 904–931.
- 497 [23] S. Berrone, S. Pieraccini, S. Scialò, An optimization approach for large scale
498 simulations of discrete fracture network flows, *J. Comput. Phys.* 256 (2014) 838–
499 853.
- 500 [24] S. Berrone, S. Pieraccini, S. Scialò, Non-stationary transport phenomena in net-
501 works of fractures: Effective simulations and stochastic analysis, *CMAME* 315
502 (2017) 1098 – 1112.

- 503 [25] S. Berrone, S. Scialò, F. Vicini, Parallel meshing, discretization, and computation
504 of flow in massive discrete fracture networks, *SISC* 41 (4) (2019) C317–C338.
- 505 [26] S. Berrone, S. Pieraccini, S. Scialò, Flow simulations in porous media with im-
506 mersed intersecting fractures, *Journal of Computational Physics* 345 (2017) 768
507 – 791.
- 508 [27] M. C. Cacas, E. Ledoux, G. De Marsily, B. Tillie, A. Barbreau, E. Durand,
509 B. Feuga, P. Peaudecerf, Modeling fracture flow with a stochastic discrete frac-
510 ture network: calibration and validation: 1. the flow model, *Water Resour. Res.*
511 26 (1990) 479–489.
- 512 [28] M. Loeve, *Probability Theory I*, Springer, 1977.
- 513 [29] S. Berrone, S. Pieraccini, S. Scialò, C. Canuto, Uncertainty quantification in dis-
514 crete fracture network models: stochastic fracture transmissivity, *Comput. Math.*
515 *Appl.* 70 (4) (2015) 603–623.
- 516 [30] L. Dedè, Reduced basis method and a posteriori error estimation for parametrized
517 linear-quadratic optimal control problems, *SISC* 32 (2) (2010) 997–1019.
- 518 [31] F. Negri, G. Rozza, A. Manzoni, A. Quarteroni, Reduced basis method for
519 parametrized elliptic optimal control problems, *SISC* 35 (5) (2013) A2316–
520 A2340.
- 521 [32] S. Berrone, S. Pieraccini, S. Scialò, Towards effective flow simulations in realistic
522 discrete fracture networks, *J. Comput. Phys.* 310 (2016) 181–201.
- 523 [33] L. J. Kenneth, M. Lilia, M. Serguei, V. Rafael, Smolyak method for solving dy-
524 namic economic models: Lagrange interpolation, anisotropic grid and adaptive
525 domain, *Journal of Economic Dynamics and Control* 44 (2014) 92 – 123.
- 526 [34] Svensk Kärnbränslehantering AB, Data report for the safety assessment sr-site,
527 tech. Rep. TR-10-52, Stockholm, Sweden (2010).